MNRAS **000**, 000–000 (0000) Preprint 27 May 2016 Compiled using MNRAS LATEX style file v3.0

The Atacama Cosmology Telescope: Dynamical masses for 44 SZ-selected galaxy clusters over 755 square degrees

Cristóbal Sifón[1,20⋆], Nick Battaglia[2], Matthew Hasselfield[3,2], Felipe Menanteau[4,5,20], L. Felipe Barrientos[6], J. Richard Bond[7], Devin Crichton[8], Mark J. Devlin[9], Rolando Dünner[6], Matt Hilton[10], Adam D. Hincks[11,12], Renée Hlozek[2], Kevin M. Huffenberger[13], John P. Hughes[14,20], Leopoldo Infante[6], Arthur Kosowsky[15], Danica Marsden[9], Tobias A. Marriage[8], Kavilan Moodley[10], Michael D. Niemack[16], Lyman A. Page[17], David N. Spergel[2], Suzanne T. Staggs[17], Hy Trac[18], Edward J. Wollack[19]

[1]*Leiden Observatory, Leiden University, PO Box 9513, NL-2300 RA Leiden, Netherlands*
[2]*Department of Astrophysical Sciences, Peyton Hall, Princeton University, Princeton, NJ 08544, USA*
[3]*Department of Astronomy and Astrophysics, Davey Lab, The Pennsylvania State University, University Park, PA, 16802, USA*
[4]*National Center for Supercomputing Applications, University of Illinois at Urbana-Champaign, 1205 W. Clark St., Urbana, IL 61801, USA*
[5]*University of Illinois at Urbana-Champaign, Department of Astronomy, 1002 W. Green Street, Urbana, IL 61801, USA*
[6]*Instituto de Astrofísica, Facultad de Física, Pontificia Universidad Católica, Casilla 306, Santiago 22, Chile*
[7]*Canadian Institute for Theoretical Astrophysics, 60 St. George, Toronto, ON M5S 3H8, Canada*
[8]*Department of Physics and Astronomy, The Johns Hopkins University, 3400 N. Charles St., Baltimore, MD 21218-2686, USA*
[9]*Department of Physics and Astronomy, University of Pennsylvania, 209 South 33rd Street, Philadelphia, PA, 19104 USA*
[10]*Astrophysics and Cosmology Research Unit, School of Mathematics, Statistics and Computer Science, University of KwaZulu-Natal, Durban 4041, South Africa*
[11]*Department of Physics and Astronomy, University of British Columbia, 6224 Agricultural Road, Vancouver, BC V6T 1Z1, Canada*
[12]*Pontificia Università Gregoriana, Piazza della Pilotta 4, 00187 Roma, Italy*
[13]*Department of Physics, Florida State University, PO Box 3064350, Tallahassee, FL 32306-4350, USA*
[14]*Department of Physics and Astronomy, Rutgers, The State University of New Jersey, 136 Frelinghuysen Road, Piscataway, NJ 08854-8019, USA*
[16]*Department of Physics, Cornell University, Ithaca, NY, 14853 USA*
[15]*Department of Physics and Astronomy, University of Pittsburgh, Pittsburgh, PA 15260, USA*
[17]*Joseph Henry Laboratories of Physics, Jadwin Hall, Princeton University, Princeton, NJ, 08544, USA*
[18]*McWilliams Center for Cosmology, Department of Physics, Carnegie Mellon University, Pittsburgh, PA 15213, USA*
[19]*NASA/Goddard Space Flight Center, Greenbelt, MD 20771, USA*

arXiv:1512.00910v2 [astro-ph.CO] 26 May 2016

27 May 2016

ABSTRACT

We present galaxy velocity dispersions and dynamical mass estimates for 44 galaxy clusters selected via the Sunyaev-Zel'dovich (SZ) effect by the Atacama Cosmology Telescope. Dynamical masses for 18 clusters are reported here for the first time. Using N-body simulations, we model the different observing strategies used to measure the velocity dispersions and account for systematic effects resulting from these strategies. We find that the galaxy velocity distributions may be treated as isotropic, and that an aperture correction of up to 7 per cent in the velocity dispersion is required if the spectroscopic galaxy sample is sufficiently concentrated towards the cluster centre. Accounting for the radial profile of the velocity dispersion in simulations enables consistent dynamical mass estimates regardless of the observing strategy. Cluster masses M_{200} are in the range $(1-15)\times10^{14}M_{\odot}$. Comparing with masses estimated from the SZ distortion assuming a gas pressure profile derived from X-ray observations gives a mean SZ-to-dynamical mass ratio of 1.10 ± 0.13, but there is an additional 0.14 systematic uncertainty due to the unknown velocity bias; the statistical uncertainty is dominated by the scatter in the mass-velocity dispersion scaling relation. This ratio is consistent with previous determinations at these mass scales.

Key words: Cosmology: observations, large-scale structure of the Universe – Galaxies: clusters: general – Galaxies: distances and redshifts

© 0000 The Authors

⋆ E-mail:sifon@strw.leidenuniv.nl

1 INTRODUCTION

Galaxy clusters are a sensitive probe of cosmology. Populating the high-end of the mass function, their number density depends strongly on the matter density in the Universe, Ω_m, and the amplitude of matter fluctuations, σ_8 (see, e.g., the review by Allen et al. 2011). Their potential as cosmological probes, however, depends critically on our knowledge of survey selection effects and baryon physics. Survey selection effects are usually properly accounted for through analytical considerations (e.g., Vikhlinin et al. 2009), numerical simulations (e.g., Sehgal et al. 2011; Sifón et al. 2013), or modeled self-consistently with scaling relations and cosmological parameters (e.g., Pacaud et al. 2007; Mantz et al. 2010; Rozo et al. 2010; Benson et al. 2013; Hasselfield et al. 2013; Bocquet et al. 2015). In contrast, incomplete knowledge of baryonic physics poses a serious and still not well understood challenge to the accuracy with which galaxy clusters can constrain cosmological parameters, and is currently the dominant systematic effect (e.g., Benson et al. 2013; Hasselfield et al. 2013).

The Sunyaev-Zel'dovich (SZ) effect (Zel'dovich & Sunyaev 1969; Sunyaev & Zeldovich 1980) is a distortion in the cosmic microwave background (CMB) temperature produced by inverse-Compton scattering of CMB photons by free electrons in the hot ($T > 10^7$ K) intracluster medium (ICM) of a galaxy cluster. The SZ effect has a distinct frequency dependence such that, in the direction of a massive cluster, the temperature of the sky increases at frequencies larger than 218 GHz while below this frequency the temperature decreases. The amplitude of this distortion is described by the line-of-sight–integrated Compton parameter, $y \propto n_e T_e$, or its solid-angle integral, $Y = \int y \, \mathrm{d}\Omega$. Its surface brightness is independent of redshift which, to first order, means that surveying the sky at millimetre wavelengths reveals all clusters above a fixed mass to high redshift, resulting in a relatively simple selection function.

Both numerical simulations (Springel et al. 2001; da Silva et al. 2004; Motl et al. 2005; Nagai 2006; Battaglia et al. 2012) and analytical studies (Reid & Spergel 2006; Afshordi 2008; Shaw et al. 2008) predict that the SZ effect should correlate with mass with low (of order 10 per cent) intrinsic scatter, although observations correlating the SZ effect with different mass proxies from X-rays (Bonamente et al. 2008; Andersson et al. 2011; Planck Collaboration 2011a; Benson et al. 2013; Rozo et al. 2014b), optical richness (High et al. 2010; Planck Collaboration 2011b; Menanteau et al. 2013; Sehgal et al. 2013), weak lensing (Hoekstra et al. 2012; Marrone et al. 2012; Planck Collaboration 2013; Gruen et al. 2014) and galaxy velocity dispersion (Sifón et al. 2013; Ruel et al. 2014; Rines et al. 2016) find a larger intrinsic scatter between mass and Y of about 20 per cent. The effect of cluster physics mentioned above, coupled to systematic effects arising from the use of different instruments (Mahdavi et al. 2013; Rozo et al. 2014a), dominate the uncertainties in these scaling relations. This uncertainty has been most notoriously highlighted by the tension in inferred cosmological parameters between the primary CMB and SZ cluster counts found by the Planck satellite (Planck Collaboration 2015a), and can be reduced by larger, more detailed analyses involving independent mass proxies and ICM tracers.

Velocity dispersions have been well studied as a proxy for galaxy cluster mass, dating back to the first such scaling relation reported by Evrard (1989), and are independent of the ICM properties that determine the SZ effect.[1] Extensive tests on numerical simulations have shown that the 3-dimensional galaxy velocity dispersion is a low-scatter mass proxy but, not surprisingly, projection effects including cluster triaxiality and large-scale structure significantly increase the scatter (White et al. 2010; Saro et al. 2013). The scatter at fixed velocity dispersion in observed samples is as large as a factor two (Old et al. 2014, 2015).[2] Importantly, the biases on these measurements (typically $\lesssim 25$ per cent for $\gtrsim 30$ observed galaxies) are much smaller than the observed scatter (Old et al. 2015), meaning that velocity dispersions remain a valuable, unbiased mass calibrator for sufficiently large cluster samples. In this paper we make use of spectroscopic data to estimate line-of-sight galaxy velocity dispersions (referred to as σ in the remainder of this section) and dynamical masses of galaxy clusters selected through their SZ effect using the Atacama Cosmology Telescope (ACT, Marriage et al. 2011b; Hasselfield et al. 2013).

In Sifón et al. (2013), we used the $\sigma - M$ scaling relation of Evrard et al. (2008) to estimate dynamical masses of a subset of these clusters. Evrard et al. (2008) calibrated this scaling relation using a suite of N-body simulations, using dark matter particles to estimate velocity dispersions. They showed that the velocity dispersions of dark matter particles in N-body simulations are robust to variations in cosmology and to different simulation codes. However, galaxies, which are used as observational tracers to measure the velocity dispersion, do not necessarily sample the same velocity distribution as the dark matter particles. Both galaxies and dark matter subhaloes (the analogues of galaxies in N-body simulations) feel dynamical friction, which distorts their velocity distribution and biases their dispersion with respect to dark matter particles. Additionally, subhaloes are tidally stripped and disrupted such that they can drop below the subhalo identification limit of a particle simulation. The lower-velocity subhaloes are more likely to be disrupted, thus the surviving subhaloes have a larger velocity dispersion which again biases the velocity dispersion of subhaloes (e.g., Faltenbacher & Diemand 2006).

The result of these effects is referred to as velocity bias, denoted $b_v \equiv \sigma_{gal}/\sigma_{DM}$ (e.g., Carlberg 1994; Colín et al. 2000). Baryonic effects are significant when quantifying the amplitude of b_v: recent high-resolution hydrodynamical simulations show significant differences in the velocity dispersions of subhaloes versus DM particles (roughly +7 per cent, which translates to a ~ 20 per cent bias in mass), but comparatively little difference between galaxies and dark matter subhaloes (e.g., Lau et al. 2010; Munari et al. 2013; Wu et al. 2013).[3] Additionally, the amplitude of b_v depends on the brightness of the observed galaxies: the velocity dispersion of brighter galaxies is generally biased low, but this can be counteracted by selecting a sample of ($\gtrsim 30$) galaxies with a representative brightness distribution (Old et al. 2013; Wu et al. 2013). In apparent contradiction with this, Guo et al. (2015a,b) used measurements of the clustering of luminous red galaxies (LRGs) to infer a *negative* velocity bias for satellite galaxies. Moreover, they found that *less*

[1] Some degree of correlation may still exist, however, because different observables are affected by the same large scale structure (White et al. 2010).
[2] In theory, the caustic technique provides a lower-scatter mass proxy than simple velocity dispersions (Gifford et al. 2013); however, it has been shown to produce similar scatter in more realistic settings (Old et al. 2014, 2015). In this respect, machine learning algorithms may become a promising alternative (Ntampaka et al. 2015b,a).
[3] Selecting galaxies by stellar mass instead of total mass reduces the strength of the velocity bias (e.g., Faltenbacher & Diemand 2006; Lau et al. 2010).

[20] Visiting Astronomer, Gemini South Observatory.

luminous LRGs have a stronger velocity bias of about 90 per cent, while more luminous LRGs have velocities consistent with those of DM particles. This result can be reconciled with those of the above simulations by noting that any given cluster[4] typically has less than ten LRGs—both Old et al. (2013) and Wu et al. (2013) find that taking the N brightest galaxies gives rise to a velocity bias of roughly 0.9, if $N \lesssim 10$.

Since observationally one uses galaxies to calculate σ, biases may be introduced if one uses a $\sigma - M$ scaling relation calibrated from simulations using dark matter particles, such as that of Evrard et al. (2008), but does not account for the aforementioned complexities. Therefore, in this paper we use the scaling relation of Munari et al. (2013), calibrated on simulated *galaxies* instead of dark matter particles, to relate velocity dispersions to cluster masses.

We present our SZ-selected cluster sample and describe the observations, data reduction and archival compilation in Section 2. In Section 3 we describe our velocity dispersion and dynamical mass estimates, including an assessment of our different observing strategies using mock observations on numerical simulations (Section 3.2), a comparison to SZ-derived masses (Section 3.5) and an investigation of cluster substructure (Section 3.6). We highlight interesting individual clusters in Section 4 and summarize the main results in Section 5.

We assume a flat ΛCDM cosmology[5] with $\Omega_m = 0.3$ and $H_0 = 70\,\mathrm{km\,s^{-1}Mpc^{-1}}$. Throughout this work we quote measurements (e.g., masses, M_Δ) at a radius r_Δ, within which the average density is Δ times the critical density of the Universe at the corresponding redshift, where $\Delta = \{200, 500\}$.

2 DATA AND OBSERVATIONS

In this section we detail the cluster sample, our follow-up observations and data processing, and archival data with which we supplement our observations. In summary, we study 44 SZ-selected clusters, of which 28 are in the celestial equator and are the focus of this paper, and 16 clusters are part of the southern survey and were studied in Sifón et al. (2013). We summarize our observing runs and sources of archival data in Table 1.

2.1 The Atacama Cosmology Telescope

The Atacama Cosmology Telescope (ACT) is a 6-meter off-axis Gregorian telescope located at an altitude of 5200 m in the Atacama desert in Chile, designed to observe the CMB at arcminute resolution. Between 2007 and 2010, ACT was equipped with three 1024-element arrays of transition edge sensors operating at 148, 218, and 277 GHz (Fowler et al. 2007; Swetz et al. 2011), although only the 148 GHz band has been used for cluster detection. In this period, ACT observed two regions of the sky, one covering 455 sq. deg. to a typical depth of 60 μK centred around declination −53° (the "southern" survey, Marriage et al. 2011b,a), and one covering 504 sq. deg. around the celestial equator, with a typical depth of 44 μK (the "equatorial" survey, Hasselfield et al. 2013). For details on the observational strategy of ACT and map making procedure see Dünner et al. (2013).

In the remainder of this section we describe ACT detections and follow-up observations of clusters in the equatorial survey. Details about the detection and optical confirmation of clusters in the southern survey can be found in Marriage et al. (2011b) and Menanteau et al. (2010), respectively. The spectroscopic observations are described in Sifón et al. (2013) and the latest SZ measurements are given in Hasselfield et al. (2013).

2.2 ACT SZ-selected clusters in the equator

Galaxy clusters were detected in the 148 GHz band by matched-filtering the maps with the pressure profile suggested by Arnaud et al. (2010), fit to X-ray selected local ($z < 0.2$) clusters, with varying cluster sizes, θ_{500}, from 1.′18 to 27′. A signal-to-noise (S/N) ratio map was extracted from each of these matched-filtered maps and all pixels with S/N > 4 were considered as cluster candidates. Cluster properties were extracted only from the map with $\theta_{500} = 5.'9$. The properties depend weakly on the exact shape of the profile as discussed in Hasselfield et al. (2013).

Because of the complete overlap of ACT equatorial observations with Sloan Digital Sky Survey Data Release 8 (SDSS DR8, Aihara et al. 2011) imaging, *all* cluster candidates were assessed with optical data (Menanteau et al. 2013). With DR8, clusters can be confidently detected up to $z \approx 0.5$. Moreover, 270 sq. deg. of the ACT survey overlap with the deep, co-added SDSS Stripe82 region (S82, Annis et al. 2014), which allows the detection of the cluster red sequence up to $z \approx 0.8$. Confirmed clusters are all those S/N > 4 candidates for which there are at least 15 galaxies within $1\,h^{-1}$ Mpc of the brightest cluster galaxy and with a photometric redshift within $0.045(1+z)$ of the cluster redshift. We additionally targeted candidate high-redshift, high S/N candidates with near infrared K_s-band imaging with the ARC 3.5m telescope at the Apache Point Observatory, which allowed us to confirm five additional clusters at $z \gtrsim 1$.[6]

A total of 68 clusters were confirmed, of which 19 (all at $z > 0.65$) were new detections. This sample has been divided into three subsamples: a complete sample of clusters within S82 at $z < 1$ and with S/N > 5 (the "cosmological" sample, containing 15 clusters), a uniform sample of 34 clusters within S82, and an incomplete sample of 19 clusters up to $z \approx 0.7$ in the shallower DR8 region. Confirmed clusters in S82 have redshifts up to $z \approx 1.3$ (with the aid of near infrared data for the higher redshifts). See Menanteau et al. (2013) for more details on the optical and infrared confirmation of clusters in the equatorial survey.

2.3 Gemini/GMOS spectroscopy

We observed 20 clusters from the equatorial sample with the Gemini Multi-Object Spectrograph (GMOS, Hook et al. 2004) on the Gemini-South telescope, split in semesters 2011B (ObsID:GS-2011B-C-1, PI:Barrientos/Menanteau) and 2012A (ObsID:GS-2012A-C-1, PI:Menanteau), prioritizing clusters in the cosmological sample at $0.3 < z < 1.0$. All observations followed our setup for the southern sample (Sifón et al. 2013). We first selected as

[4] Note that both the simulations and the observations of Guo et al. (2015a,b) refer to clusters with masses well below $10^{15}\mathrm{M}_\odot$.

[5] Assuming Planck-level uncertainties in Ω_m and H_0 (Planck Collaboration 2015b) introduces a < 5 per cent difference in the reported masses, accounting for their influence on both member selection (through changes in projected physical distances) and the adopted scaling relation.

[6] One of these clusters, ACT-CL J0012.0−0046, associated with an overdensity of red galaxies at $z = 1.36$ by Menanteau et al. (2013), is detected at much lower significance in new, more sensitive SZ observations performed with ACTPol (M. Hilton et al., in prep).

Table 1. Summary of spectroscopic observations and sources of archival data. The last column lists the number of clusters observed in each program. Previously published data have the corresponding references. All SDSS clusters have been observed by us in one of the listed programs as well.

Instrument / Archival source	Semester	Program	PI	Data reference	Sample	N_{cl}
VLT/FORS2	2009B	084.A-0577	Infante	Sifón et al. (2013)	South	3
	2010B	086.A-0425	Infante	Sifón et al. (2013)	South	2
Gemini/GMOS	2009B	GS-2009B-Q-2	Barrientos	Sifón et al. (2013)	South	4
	2010B	GS-2010B-C-2	Barrientos/Menanteau	Sifón et al. (2013)	South	10
	2011B	GS-2011B-C-1	Barrientos/Menanteau	this work	Equator	12
	2012A	GS-2012A-C-1	Menanteau	this work	Equator	8
SALT/RSS	2012A	2012-1-RSA_UKSC_RU-001	Hilton/Hughes	Kirk et al. (2015)	Equator	1
	2012B	2012-2-RSA_UKSC_RU-001	Hilton/Hughes	Kirk et al. (2015)	Equator	2
	2013A	2013-1-RSA_RU-001	Hilton/Hughes	Kirk et al. (2015)	Equator	1
	2013B	2013-2-RSA_RU-002	Hilton/Hughes	Kirk et al. (2015)	Equator	3
SDSS DR12	–	–	–	Alam et al. (2015)	Equator	20
HeCS	–	–	–	Rines et al. (2013)	Equator	3
NED	–	–	–	Soucail et al. (1988), Dressler et al. (1999)	Equator	1

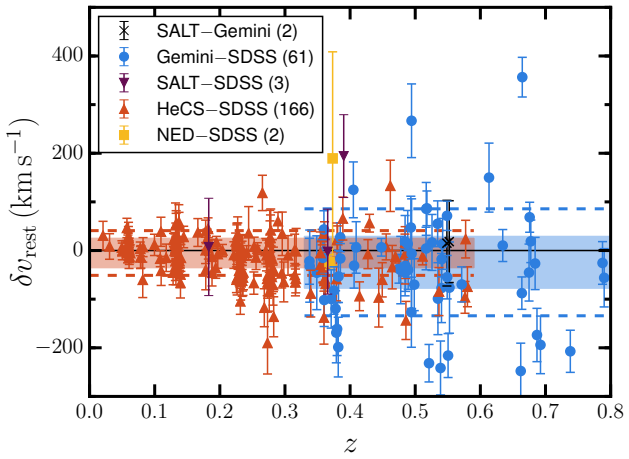

Figure 1. Comparison of redshifts from all spectroscopic datasets to SDSS measurements (for overlapping galaxies), shown as $\delta v_{\rm rest} = c\,(z_1 - z_2)/(1 + z_2)$, where $z_2 = z_{\rm SDSS}$ (except for the black crosses, where $z_2 = z_{\rm Gemini}$). All redshifts are in the heliocentric frame. Red, yellow, purple and blue points correspond to redshifts from the HeCS survey (Rines et al. 2013), from NED for Abell 370, and from our SALT/RSS and Gemini/GMOS campaigns, respectively, while black crosses compare our redshift measurements between SALT/RSS and Gemini/GMOS. Individual uncertainties correspond to the quadrature sum of the uncertainties from both measurements. Red and blue shaded regions show uncertainties on the weighted means for HeCS−SDSS and Gemini−SDSS, respectively, and dashed horizontal lines show standard deviations. The number of matches per data set pair are given in parentheses in the legend.

targets those galaxies with photometric redshifts within $\Delta z = 0.1$ of the cluster photometric redshift and prioritized bright galaxies as allowed by the multi-object spectroscopy (MOS) masks. The only major difference in strategy from Sifón et al. (2013) is that, owing to the SDSS photometry, we targeted galaxies out to larger radii than in the southern observations, in which we were bound by the roughly 5′ fields of view of our targeted optical follow-up with 4m-class telescopes (Menanteau et al. 2010). We followed this approach because of the indication, especially from numerical simulations, that the velocity dispersion is a decreasing function of radius; therefore an unbiased velocity dispersion estimate is predicted only if galaxies are sampled out to approximately the cluster's virial radius (e.g., Girardi et al. 1998; Biviano et al. 2006; Mamon et al. 2010). We observed 2-3 masks per cluster along the (visually identified) major axis of the galaxy distribution. In order to obtain a wide sky coverage, these masks were mostly non-overlapping in the sky, even though this meant we had fewer targets per unit area. We detail the differences with the southern strategy, and address the impact of these differences in our measurements, in Section 3.2.

We used `pygmos`[7] (Sifón et al. 2013), an automated Python/PyRAF script[8] that goes from raw data to one-dimensional spectra, including bias subtraction, flat field correction, wavelength calibration, cosmic ray rejection (van Dokkum 2001) and sky subtraction. Redshifts[9] were measured by cross-correlating the spectra with template spectra from SDSS[10] using XCSAO within IRAF's RVSAO package[11] (Kurtz & Mink 1998).

2.4 SALT/RSS spectroscopy

We also observed seven clusters in S82 with the Robert Stobie Spectrograph (RSS, Burgh et al. 2003) on the Southern African Large Telescope (SALT), using multi-object spectroscopy. Details of these observations are given in Kirk et al. (2015). Target selection and redshift measurements were carried in a similar, but not identical, fashion to the GMOS observations of the equatorial clusters. The data were prepared with `pysalt` (Crawford et al. 2010), after which they were reduced with standard IRAF[12] functions. Redshift measurements are also obtained with XCSAO. ACT-CL J0045.2−0152 is the only cluster that was observed both with Gemini and SALT, but there are only two galaxies in our final catalogue observed with both telescopes.

[7] http://www.strw.leidenuniv.nl/~sifon/pygmos/
[8] PyRAF is a product of the Space Telescope Science Institute, which is operated by AURA for NASA.
[9] All redshifts presented here are in the heliocentric frame.
[10] http://www.sdss.org/DR7/algorithms/spectemplates/index.html
[11] http://tdc-www.harvard.edu/iraf/rvsao/
[12] http://iraf.noao.edu/

2.5 Archival data

In order to enlarge the sample of studied clusters and member galaxies, we also compiled archival data for the equatorial sample. Specifically, we searched the SDSS Data Release 12 (DR12, Alam et al. 2015) database[13]. We retrieved all galaxies with a valid redshift (that is, `z>0` and `zWarning=0`) within a cluster-centric distance of 20′ (corresponding to several times r_{200} for most clusters) and found a total of 2001 galaxies (most of which are not cluster members; see Section 3) in the direction of 25 of the ACT equatorial clusters observed with Gemini or SALT. Of the galaxies with SDSS spectra, 61 were also observed by us with Gemini, and three with SALT. We compare these repeat observations in Section 2.6. There are additionally four clusters in the equatorial sample with dedicated archival observations; we did not observe any of these clusters ourselves. We briefly describe these data below.

The Hectospec Cluster Survey (HeCS, Rines et al. 2013) was designed to measure the masses of galaxy clusters at $0.1 < z < 0.3$ out to the infall regions of clusters (typically around $4r_{200}$), targeting more than four hundred objects per cluster within a radius of 30′ (corresponding to 6 Mpc at $z = 0.2$). The three clusters below $z = 0.3$ in the cosmological sample of Hasselfield et al. (2013) were targeted by Rines et al. (2013), namely ACT-CL J0152.7+0100 (Abell 267), ACT-CL J2129.6+0005 (RX J2129.6+0005) and ACT-CL J2337.6+0016 (Abell 2631). We include these three clusters in our analysis. Rines et al. (2013) also measured redshifts using XCSAO; we use only galaxies with redshift quality flags `'Q'` or `'?'`, which correspond to secure redshifts for high- and medium-quality spectra, respectively (Rines et al. 2013).

Additionally, the cluster ACT-CL J0239.8−0134 ($z = 0.375$) is the well-studied, HST Frontier Fields[14] cluster Abell 370. Despite extensive lensing studies (e.g. Medezinski et al. 2010; Richard et al. 2010; Hoekstra et al. 2012; von der Linden et al. 2014a), there is no modern spectroscopic data on this cluster. A search in the NASA/IPAC Extragalactic Database[15] (NED) gives roughly 100 galaxies with redshifts in the range $0.30 \leqslant z \leqslant 0.45$, which safely includes all potential cluster members (we then run our membership algorithm on these galaxies, see Section 3.1). These galaxies go out to 6′ in radius. For homogeneity, we limit ourselves to redshifts measured either by Soucail et al. (1988) or Dressler et al. (1999) since these two sources make up the majority ($\approx$ 90 per cent) of galaxies returned by NED. We assign to each galaxy an uncertainty at the level of the last non-zero digit.

2.6 Comparison between redshift measurements

There are many overlapping galaxies between SDSS and other data, as well as two overlapping galaxies between our SALT/RSS and Gemini/GMOS observations of ACT-CL J0045.2−0152. We compare the spectroscopic redshifts between the different measurements in Figure 1. There is good agreement between the different datasets. In particular, the inverse-variance-weighted average differences in rest-frame velocity (defined as $\delta v_{\rm rest} = c\,(z_1 - z_2)/(1+z_2)$) are $\delta v_{\rm rest} = -24.2 \pm 53.1\,{\rm km\,s^{-1}}$ (where the errorbar is the uncertainty on the mean) between GMOS and SDSS, with a standard deviation $\sigma_{\delta v} = 110\,{\rm km\,s^{-1}}$, and $\delta v_{\rm rest} = -5.1 \pm 30.0\,{\rm km\,s^{-1}}$ between HeCS and SDSS, with $\sigma_{\delta v} = 46\,{\rm km\,s^{-1}}$. The standard deviations are 2.07 and 1.39 times the average XCSAO errors, respectively. We conclude that XCSAO underestimates the true cross-correlation velocity uncertainty by up to a factor two, consistent with previous determinations (e.g., Quintana et al. 2000; Boschin et al. 2004; Barrena et al. 2009). HeCS spectra have a higher S/N than GMOS spectra; therefore it is possible that the level of underestimation depends on the S/N of the spectrum.

3 VELOCITY DISPERSIONS AND DYNAMICAL MASSES

3.1 Velocity dispersion measurements

We use the shifting gapper method developed by Fadda et al. (1996) as implemented in Sifón et al. (2013) to select cluster members, as follows. Assuming the BCG to correspond to the cluster centre[16] (the impact of this assumption is assessed in Section 3.7), we bin galaxies by their (projected) cluster-centric distance in bins of at least 250 kpc and 10 galaxies. Therefore member selection in clusters with fewer than 20 redshifts was performed using a single bin (i.e., a standard sigma-clipping). A visual inspection of the phase-space diagrams of clusters with few members suggests that this choice is better than the 15 galaxies used in Sifón et al. (2013), where clusters had an average 65 members over a smaller area of the sky.[17] In each bin in projected distance we sort galaxies by the absolute value of their peculiar velocity (taken initially with respect to the median redshift of potential cluster members). In practice, this means we assume that clusters are symmetric in the radial direction. We then select a main body of galaxies having peculiar velocities $|v_i| < |v_{i-1}| + 500\,{\rm km\,s^{-1}}$, where the index i runs over all galaxies in a given radial bin. In other words, the main body is composed, in each radial bin, by the group of galaxies intersecting $v = 0$ and bound by velocity differences of less than $500\,{\rm km\,s^{-1}}$. All galaxies with peculiar velocities less than $1000\,{\rm km\,s^{-1}}$ away from the main body are considered cluster members. Modifying the velocity gaps does not have a noticeable impact on our results—all clusters have well defined boundaries in velocity space. This process is iterated, updating the cluster redshift and the radial binning, until the number of members converges (usually two to three iterations).

At every step in the member selection process, cluster redshifts and velocity dispersions are calculated as the biweight estimators of location and scale (i.e., the central value and dispersion, respectively, see equations 5 and 9 of Beers et al. 1990), respectively. We correct the velocity dispersion for individual redshift uncertainties (Danese et al. 1980), but this is a < 1 per cent correction for $\sigma = 1000\,{\rm km\,s^{-1}}$. We estimate 68 per cent uncertainties in cluster redshifts and velocity dispersions by bootstrapping over all galaxies within 3σ of the measured velocity dispersion, which is always larger than the velocity limit defined by the shifting gapper. Therefore we include galaxies which are rejected by our member selection algorithm, and thus account for uncertainties arising from membership selection in the redshift and velocity dispersion uncertainties. We find that the membership selection process increases the statistical uncertainties in the mass by a median 2 per cent for

[13] http://skyserver.sdss9.org/public/en/home.aspx
[14] http://www.stsci.edu/hst/campaigns/frontier-fields/
[15] http://ned.ipac.caltech.edu

[16] The only exception is ACT-CL J2302.5+0002, which we discuss in Section 4.6.
[17] The difference in the dynamical masses (which are reported in Section 3.4) between using 10 or 15 galaxies as a minimal bin size in the shifting gapper is six per cent, well within the reported errorbars.

the full sample (but by > 20 per cent for nine clusters where a large number of objects are rejected by the member selection algorithm). Such a small value is dominated by the southern clusters where, since we targeted the central regions only, the number of galaxies rejected by our algorithm is small compared to the number of members (only 2 per cent, compared to 24 per cent of galaxies rejected for the equatorial clusters). For comparison, we also implement a Bayesian algorithm to estimate velocity dispersions statistically accounting for an interloper component with constant spatial density (Wojtak et al. 2007; Andreon et al. 2008). The Bayesian analysis yields velocity dispersions, as well as uncertainties, that are consistent with our analysis.

Cluster redshifts and velocity dispersions are listed in Table 2. We show velocity histograms of clusters in the equatorial and southern samples in Figures B1 and B2, respectively.

3.2 Calibrating velocity dispersions with the Multidark simulation

To estimate a possible bias in the velocity dispersions arising from the different optical observations, especially between our southern and equatorial campaigns, we use mock observations of dark matter haloes in the Multidark simulation (Prada et al. 2012). Here we want to understand whether there is a relative bias between the two strategies compared to the "true" velocity dispersion. By "true" we mean the line-of-sight velocity dispersion obtained using all the subhaloes found in the simulation within r_{200}, where r_{200} is measured directly in the simulation as the distance from the centre of mass within which the density is 200 times the critical density. We begin by describing the Multidark simulation and then describe our mock observations of subhaloes that follow our real observing strategies.

We used haloes from the Multidark BDMW database (Riebe et al. 2013) constructed from the N-body Multidark MDPL simulation (Prada et al. 2012). The Multidark simulation is an N-body simulation containing 3840^3 dissipationless particles in a box of length $1\,h^{-1}$Gpc and run using a variation of the GADGET2 code (Springel 2005). The halo catalog was constructed using a spherical over-density halo finder that used the bound density maxima algorithm (BDM, Klypin & Holtzman 1997) with an over-density criterion of 200 times the critical density of the Universe. The cosmology used in the simulation is a concordance ΛCDM model that is consistent with Planck Collaboration (2014); the parameters are $\Omega_\Lambda = 0.69$, $\Omega_\mathrm{m} = 0.31$, $\Omega_\mathrm{b} = 0.048$, $h = 0.68$, and $\sigma_8 = 0.82$. The small differences in cosmological parameters between the simulations and those adopted by us ($\Omega_\mathrm{m} = 0.3$, $h = 0.7$) have no impact on our results.

We select all haloes at $z = 0$ more massive than $10^{14}\,h^{-1}\mathrm{M}_\odot$ and containing a minimum number of 50 subhaloes more massive than $10^{12}\,h^{-1}\mathrm{M}_\odot$. A total of 572 haloes meet these criteria. We created mock observations of the Multidark haloes by implementing distinct algorithms for the southern and equatorial strategies to mimic our observational strategies. While the southern campaign was confined to areas $\approx 5' \times 5'$ around the BCGs, for the equatorial sample we tried to observe as far out as possible (see Section 2.3). First, we scaled projected distances of the subhaloes to $z = 0.5$, the median redshift of our sample. As our sample spans $0.25 < z < 1.06$, an observing field of fixed angular extent contains different fractions of r_{200}. However, as we show below, the most important parameter is the radial coverage. There is therefore no extra information in scaling distances to different redshifts.

We note that our goal in this section is not to test the membership selection algorithm, and we therefore only include subhaloes in Multidark within r_{200}. Unbound subhaloes may appear to be part of a cluster in projection, and this can bias velocity dispersion measurements. However, the same member selection and velocity dispersion algorithms used here were applied to mock catalogs including this 'interloper' population in Old et al. (2015), who showed that despite this our method is able to recover unbiased mass measurements. Instead, we aim to assess any intrinsic, *relative* biases introduced in our sample by having different observing strategies. We account for the impact of these projection effects as a systematic uncertainty in our final estimate of the dynamical mass uncertainties (see Section 3.4).

To simulate the southern observations, we observed up to 70 galaxies in the inner $5' \times 5'$ randomly. Given the resolution of Multidark, we were typically able to "observe" 45 subhaloes following this strategy. To recreate the equatorial observations we first identified the approximate major axis of the subhalo distribution for each cluster by taking the mean direction of the 10 largest distances between cluster members. We then created a MOS mask with slits of length $8''$ along this major axis (axis x' as per the right panel of Figure 2), and observed exactly one subhalo in each slit (unless there were no subhaloes in the slit area). To define which subhalo to "observe," we selected an object from each slit with a Gaussian distribution around the cluster major axis such that we preferentially, but not exclusively, observed subhaloes close to the line passing through the central subhalo (representing the BCG). This setup led to, on average, 25 subhaloes observed per cluster for the equatorial strategy. Figure 2 illustrates our southern and equatorial spectroscopic strategies applied to a halo of the Multidark simulation. Because the number of "observed" subhaloes per halo is lower than the number of observed galaxies per cluster, the statistical uncertainties in the velocity dispersions from the mock observations overestimate the measured uncertainties per cluster. This, however, does not compromise our assessment of a bias introduced by either strategy, and is compensated by the large number of simulated haloes used. We note that the strategies defined above are generalizations (e.g., some clusters in the equator have denser sampling and out to smaller radii). We apply the relevant corrections (see below) to all clusters irrespective of the sample they belong to (that is, southern or equatorial sample), solely based on their particular observational setup.

The residuals in the recovered velocity dispersions with respect to the true halo velocity dispersion (i.e., that determined using all subhaloes, typically 60) are shown in Figure 3 for each observational strategy. As a consistency check, we also show the residuals determined from measuring the velocity dispersion from all subhaloes within r_{200}, as determined iteratively from the mock observations following the procedure described in Section 3.1, which are consistent with the true velocity dispersions within the statistical uncertainty. This comparison shows that the adopted scaling relation (see Section 3.3) is consistent with the scaling of Multidark haloes and that, in an ideal case where we observe all subhaloes, our estimates of both σ_{200} and r_{200} (and thereby M_{200}) are unbiased.

Figure 3 also shows the distribution of velocity dispersions recovered from the simulations for both our observing strategies. For the equatorial strategy the velocity dispersions are unbiased, meaning that the velocity distributions are well sampled within the statistical precision we require—there is no bias introduced by sampling galaxies along a particular direction (but see Skielboe et al. 2012, for evidence of a preferred direction for the velocity distribution in galaxy clusters). The velocity distribution derived from the

Table 2. Redshifts, velocity dispersions and dynamical masses of ACT SZ-selected clusters. The horizontal line separates equatorial and southern clusters. Clusters in the cosmological samples of Hasselfield et al. (2013) have a "Cosmo" suffix in the second column. The third and fourth columns give the total number of members, $N_{\rm m}$, and the number of members within r_{200}, N_{200}. We list the maximum radius at which we have spectroscopic members, $r_{\rm max}$, and the velocity dispersion of all members, $\sigma(< r_{\rm max})$, as well as the quantities calculated specifically within r_{200}. Uncertainties in the masses do not include the scatter in the $\sigma - M$ scaling relation. Alternative cluster names are given in Menanteau et al. (2013).

Cluster	Sample	$N_{\rm m}$	N_{200}	$z_{\rm cl}$	$\sigma(< r_{\rm max})$ (km s^{-1})	$r_{\rm max}$ (r_{200})	σ_{200} (km s^{-1})	r_{200} (Mpc)	M_{200} (10^{14} M$_\odot$)
ACT-CL J0014.9−0057	S82-Cosmo	62	45	0.5331 ± 0.0007	806 ± 91	1.75	850 ± 108	1.31 ± 0.16	4.5 ± 1.6
ACT-CL J0022.2−0036	S82-Cosmo	55	44	0.8048 ± 0.0014	961 ± 124	1.71	1025 ± 164	1.33 ± 0.20	6.6 ± 3.0
ACT-CL J0045.2−0152	DR8	56	44	0.5483 ± 0.0010	930 ± 77	1.40	967 ± 88	1.45 ± 0.12	6.3 ± 1.6
ACT-CL J0059.1−0049	S82-Cosmo	44	23	0.7870 ± 0.0012	884 ± 150	1.82	874 ± 206	1.19 ± 0.28	4.6 ± 3.2
ACT-CL J0119.9+0055	S82	16	14	0.7310 ± 0.0011	725 ± 128	1.06	786 ± 149	1.10 ± 0.20	3.4 ± 1.9
ACT-CL J0127.2+0020	S82	46	46	0.3801 ± 0.0008	994 ± 106	0.92	991 ± 108	1.64 ± 0.17	7.5 ± 2.3
ACT-CL J0152.7+0100	S82-Cosmo	253	144	0.2291 ± 0.0004	931 ± 41	2.57	1065 ± 54	1.89 ± 0.09	9.7 ± 1.4
ACT-CL J0206.2−0114	S82-Cosmo	40	23	0.6758 ± 0.0010	570 ± 105	2.02	625 ± 164	0.94 ± 0.25	2.0 ± 1.6
ACT-CL J0215.4+0030	S82-Cosmo	14	11	0.8622 ± 0.0026	1386 ± 262	1.27	1256 ± 268	1.57 ± 0.33	11.7 ± 7.3
ACT-CL J0218.2−0041	S82-Cosmo	61	41	0.6727 ± 0.0008	723 ± 76	1.80	790 ± 92	1.12 ± 0.12	3.4 ± 1.1
ACT-CL J0219.9+0129	DR8	10	10	0.3651 ± 0.0014	1001 ± 224	0.56	963 ± 215	1.66 ± 0.36	7.6 ± 5.0
ACT-CL J0223.1−0056	S82-Cosmo	38	27	0.6632 ± 0.0011	829 ± 96	1.25	911 ± 165	1.31 ± 0.23	5.3 ± 2.8
ACT-CL J0239.8−0134	DR8	75	75	0.3751 ± 0.0009	1216 ± 128	0.64	1183 ± 128	1.94 ± 0.19	12.2 ± 3.7
ACT-CL J0241.2−0018	S82	36	26	0.6872 ± 0.0013	830 ± 132	1.70	905 ± 160	1.28 ± 0.22	5.1 ± 2.6
ACT-CL J0256.5+0006	S82-Cosmo	78	78	0.3625 ± 0.0008	1185 ± 102	0.59	1144 ± 102	1.89 ± 0.16	11.2 ± 2.8
ACT-CL J0320.4+0032	S82	25	25	0.3847 ± 0.0014	1284 ± 209	0.56	1236 ± 215	2.03 ± 0.34	14.3 ± 7.1
ACT-CL J0326.8−0043	S82-Cosmo	62	59	0.4471 ± 0.0006	897 ± 96	1.21	927 ± 101	1.49 ± 0.15	6.0 ± 1.8
ACT-CL J0342.7−0017	S82	19	19	0.3072 ± 0.0015	941 ± 173	0.80	930 ± 173	1.64 ± 0.29	6.9 ± 3.7
ACT-CL J0348.6−0028	S82	15	15	0.3449 ± 0.0010	642 ± 117	0.51	614 ± 112	1.10 ± 0.19	2.2 ± 1.1
ACT-CL J2050.5−0055	S82-Cosmo	33	14	0.6226 ± 0.0007	539 ± 120	2.32	511 ± 97	0.79 ± 0.14	1.1 ± 0.6
ACT-CL J2050.7+0123	DR8	47	47	0.3339 ± 0.0009	1046 ± 104	0.92	1043 ± 103	1.76 ± 0.16	8.8 ± 2.4
ACT-CL J2055.4+0105	S82	55	52	0.4089 ± 0.0005	759 ± 77	1.11	778 ± 78	1.29 ± 0.12	3.8 ± 1.1
ACT-CL J2058.8+0123	DR8	16	16	0.3285 ± 0.0014	1109 ± 196	0.65	1080 ± 191	1.86 ± 0.31	10.2 ± 5.2
ACT-CL J2128.4+0135	DR8	59	56	0.3856 ± 0.0006	895 ± 116	1.12	906 ± 119	1.51 ± 0.19	5.9 ± 2.2
ACT-CL J2129.6+0005	S82-Cosmo	291	68	0.2337 ± 0.0005	786 ± 39	5.05	859 ± 91	1.56 ± 0.15	5.5 ± 1.6
ACT-CL J2154.5−0049	S82-Cosmo	52	42	0.4904 ± 0.0011	918 ± 108	1.42	964 ± 121	1.51 ± 0.18	6.6 ± 2.3
ACT-CL J2302.5+0002	S82	47	39	0.5199 ± 0.0007	648 ± 67	1.16	671 ± 63	1.06 ± 0.11	2.4 ± 0.7
ACT-CL J2337.6+0016	S82-Cosmo	154	51	0.2769 ± 0.0007	853 ± 52	4.85	879 ± 96	1.56 ± 0.16	5.7 ± 1.7
ACT-CL J0102−4915	South-Cosmo	86	81	0.8700 ± 0.0010	1273 ± 114	1.18	1284 ± 117	1.55 ± 0.13	11.3 ± 2.9
ACT-CL J0215−5212	South	54	54	0.4803 ± 0.0009	1027 ± 110	0.83	1018 ± 111	1.59 ± 0.16	7.6 ± 2.3
ACT-CL J0232−5257	South	63	63	0.5561 ± 0.0007	924 ± 87	0.66	900 ± 86	1.35 ± 0.12	5.2 ± 1.4
ACT-CL J0235−5121	South	80	80	0.2775 ± 0.0005	1044 ± 93	0.48	994 ± 92	1.74 ± 0.15	8.0 ± 2.0
ACT-CL J0237−4939	South	65	65	0.3343 ± 0.0007	1290 ± 91	0.39	1210 ± 91	2.01 ± 0.14	13.1 ± 2.7
ACT-CL J0304−4921	South	61	61	0.3917 ± 0.0007	1098 ± 98	0.51	1050 ± 96	1.71 ± 0.15	8.7 ± 2.2
ACT-CL J0330−5227	South-Cosmo	71	71	0.4417 ± 0.0008	1247 ± 96	0.46	1182 ± 98	1.85 ± 0.14	11.6 ± 2.7
ACT-CL J0346−5438	South	88	88	0.5297 ± 0.0007	1081 ± 76	0.77	1066 ± 75	1.60 ± 0.10	8.3 ± 1.6
ACT-CL J0438−5419	South-Cosmo	63	63	0.4212 ± 0.0009	1268 ± 109	0.56	1221 ± 108	1.93 ± 0.16	12.9 ± 3.2
ACT-CL J0509−5341	South-Cosmo	74	71	0.4601 ± 0.0005	860 ± 79	1.13	865 ± 82	1.38 ± 0.12	4.9 ± 1.3
ACT-CL J0521−5104	South	19	19	0.6742 ± 0.0018	941 ± 194	0.97	940 ± 198	1.35 ± 0.28	5.9 ± 3.6
ACT-CL J0528−5259	South	55	44	0.7676 ± 0.0010	934 ± 114	1.45	984 ± 125	1.30 ± 0.16	5.9 ± 2.1
ACT-CL J0546−5345	South-Cosmo	45	40	1.0668 ± 0.0013	1020 ± 138	1.20	1018 ± 148	1.13 ± 0.15	5.5 ± 2.3
ACT-CL J0559−5249	South-Cosmo	25	25	0.6094 ± 0.0016	1085 ± 136	0.86	1078 ± 137	1.55 ± 0.19	8.3 ± 3.0
ACT-CL J0616−5227	South-Cosmo	18	18	0.6837 ± 0.0015	1156 ± 193	0.75	1139 ± 190	1.58 ± 0.25	9.5 ± 4.5
ACT-CL J0707−5522	South	58	58	0.2958 ± 0.0005	838 ± 82	0.66	816 ± 83	1.44 ± 0.14	4.6 ± 1.3

southern strategy is, on the other hand, biased by 0.02 dex (corresponding to ≈ 5 per cent) on average, which is consistent with the picture of a decreasing velocity dispersion outward from the cluster centre (e.g., Mamon et al. 2010). We correct for this bias by measuring the *true* integrated velocity dispersion profiles for Multidark haloes and scaling them up to $\sigma_{200} \equiv \sigma(r = r_{200})$. We list the radial correction $\sigma(< r)/\sigma_{200}$ and the associated scatter in Table 3, and show it in Figure 4. While the spread increases towards small apertures, the correction is < 10 per cent at all radii. However, at small radii the scatter is large and must be included in the error estimate when measuring velocity dispersions. We apply this correction to each halo when observed with the southern strategy and are able to recover unbiased velocity dispersions (see Figure 3).

3.3 From velocity dispersions to dynamical masses

In Sifón et al. (2013), we used the $\sigma - M_{200}$ scaling relation of Evrard et al. (2008) to estimate dynamical masses. As discussed in Section 1, the scaling relation of Evrard et al. (2008) was calibrated from a suite of N-body simulations using dark matter particles to

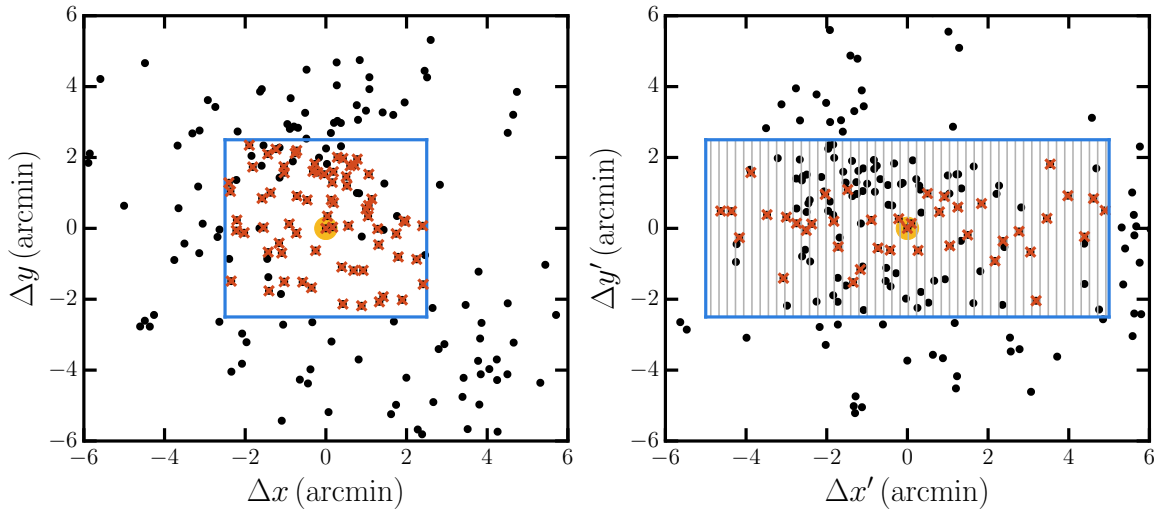

Figure 2. The two simulated observational strategies, for a Multidark halo of mass $M_{200} = 1.76 \times 10^{15} M_\odot$. The same halo is shown in both panels; in the right panel axes are rotated such that the slits are placed along the horizontal axis. Angular distances are scaled to $z = 0.5$; at this redshift, the size r_{200} of this halo corresponds to 7′.6.. Black dots are all halo members, of which red crosses are used to calculate the velocity dispersion. The orange circle in the middle marks the central subhalo, which is always used to calculate the velocity dispersion, and the blue rectangle outlines the field of view. *Left:* the southern strategy, in which we observed up to 70 randomly selected members in the central $5' \times 5'$. *Right:* the equatorial strategy, in which we observed an average 25 members inside a $10' \times 5'$ field of view along the major axis of the subhalo distribution. Grey vertical stripes show the mask slit boundaries, and only one galaxy is observed per slit.

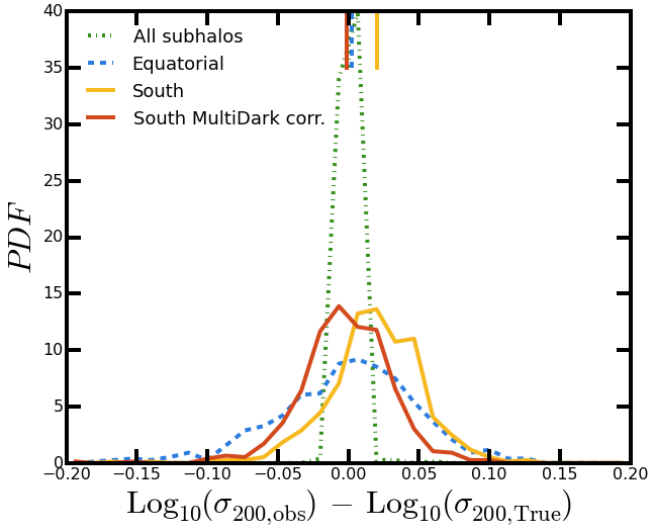

Figure 3. Probability distribution functions of the residuals between the measured and true velocity dispersions in the Multidark simulation, in logarithmic space. The dash-dotted green, dashed blue, and solid yellow lines show the differences using all subhaloes, an average of 25 subhaloes with the equatorial strategy, and an average of 45 subhaloes with the southern strategy, respectively. The red solid line shows the residuals in the southern strategy after correcting for incomplete sky coverage (see Section 3.2). Vertical lines at the top of the figure show the median values.

estimate velocity dispersions. However, the galaxies, from which velocity measurements are made in reality do not sample the same velocity distribution as the dark matter (hereafter DM) particles. They feel dynamical friction and some are tidally disrupted, which distorts their velocity distribution and biases their dispersion (e.g., Carlberg 1994; Colín et al. 2000). Recent high resolution hydrodynamical simulations of "zoomed" cosmological haloes have shown

Table 3. Ratio of one-dimensional velocity dispersion within an aperture r, $\sigma(< r)$, to the one-dimensional velocity dispersion within r_{200}, σ_{200}, estimated using subhaloes in the Multidark simulation. Uncertainties are the standard deviations. These values are plotted in Figure 4.

r/r_{200}	$\langle\sigma(< r)/\sigma_{200}\rangle$
0.2	1.03 ± 0.27
0.3	1.07 ± 0.17
0.4	1.06 ± 0.11
0.5	1.05 ± 0.08
0.6	1.03 ± 0.05
0.7	1.02 ± 0.04
0.8	1.01 ± 0.02
0.9	1.00 ± 0.01
1.0	1.00 ± 0.00

that there is a significant difference between the velocity distributions of DM particles and galaxies themselves; whether galaxies (i.e., overdensities of stars in hydrodynamical simulations) or dark matter subhaloes are used makes comparatively little difference (Munari et al. 2013). Results from state-of-the art numerical simulations depend on the exact definition of a galaxy and the member selection applied, but the current consensus is that galaxies are biased high (i.e., at a given mass the velocity dispersion of galaxies or subhaloes is larger than that of DM particles) by 5–10 per cent with respect to DM particles (Lau et al. 2010; Munari et al. 2013; Wu et al. 2013), translating into a positive 15–20 per center bias in dynamical masses when using DM particles. This is illustrated in Figure 5: DM particles are not significantly impacted by either dynamical friction or baryonic physics; therefore the scaling relations for DM particles are essentially the same for all simulations. In contrast, dark matter subhaloes are affected by baryons in such a way that including baryonic feedback (most importantly feedback from active galactic nuclei (AGN), but also from cooling and star forma-

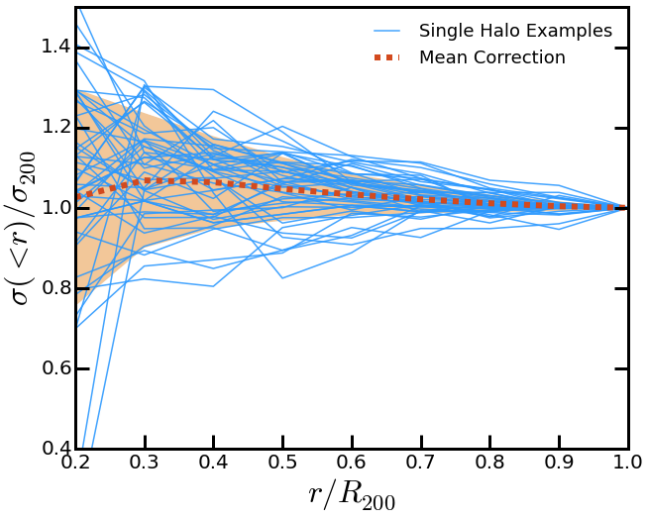

Figure 4. Enclosed one-dimensional velocity dispersion, $\sigma(< r)$, as a function of radius, r, for subhaloes in Multidark, normalized to σ_{200} and r_{200}, respectively. The red dashed line is the mean value, and the orange region encloses 68 per cent of the haloes. Blue lines are a random subset of the Multidark haloes. The data for this figure are presented in Table 3.

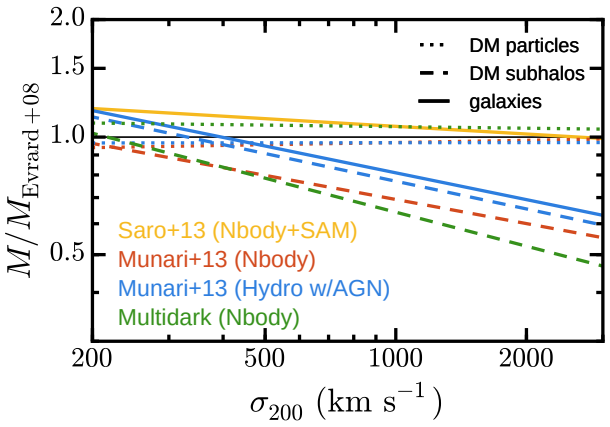

Figure 5. Comparison between different $\sigma - M$ scaling relations, relative to the scaling relation of dark matter particles derived by Evrard et al. (2008). Dotted, dashed and solid lines show scaling relations for dark matter particles, dark matter subhaloes and galaxies, respectively. We show the scaling relation for galaxies derived from a semi-analytic model implemented in a dark matter-only simulation by Saro et al. (2013) in yellow. Red and blue lines show the scaling relations derived from dark matter-only and full hydrodynamical simulations, respectively, by Munari et al. (2013), and the green lines show scaling relations from the Multidark simulation. In this work, we calculate dynamical masses using the scaling relation given by the blue solid line.

tion) makes their velocity dispersions much more similar to those of simulated galaxies. This means we can rely on our analysis of the previous section, based on dark matter subhaloes, to correct the velocity dispersions measured for ACT clusters, and then estimate dynamical masses using predictions obtained either from galaxies or subhaloes. The difference between the Saro et al. (2013) and Munari et al. (2013) galaxy scaling relations depends on the details of the semi-analytic and hydrodynamical implementations used in Saro et al. (2013) and Munari et al. (2013), respectively. The different cosmologies used in the Millenium simulation (in particular, $\sigma_8 = 0.9$; Springel et al. 2005) by Saro et al. (2013) and the simulations by Munari et al. (2013) ($\sigma_8 = 0.8$) may also play a role.

We therefore use the scaling relation between the projected galaxy velocity dispersion and mass estimated by Munari et al. (2013), obtained from zoomed-in hydrodynamical simulations of dark matter haloes, that includes prescriptions for cooling, star formation, and AGN feedback,

$$\sigma_{200} = A_{1D} \left[\frac{h\, E(z)\, M_{200}}{10^{15} \mathrm{M}_\odot} \right]^{\alpha} \quad (1)$$

where σ_{200} is the 3-dimensional velocity dispersion of galaxies within r_{200}, divided by $\sqrt{3}$ (i.e., the line-of-sight velocity dispersion in a spherical cluster), $E(z) = [\Omega_\Lambda + (1+z)^3\Omega_{\rm m}]^{1/2}$, $A_{1D} = 1177 \pm 4.2\,\mathrm{km\,s^{-1}}$, and $\alpha = 0.364 \pm 0.002$. The intrinsic scatter *at fixed mass* in Equation 1 is of order 5 per cent, or ≈15 per cent in mass (Munari et al. 2013), but this value does not include the effect of interlopers (that is, impurity in the member sample), which can increase the intrinsic scatter by up to a factor two (Biviano et al. 2006; Mamon et al. 2010; White et al. 2010; Saro et al. 2013). This is an irreducible uncertainty since there is always a fraction of contaminating galaxies that cannot be identified by their peculiar velocities because they overlap with the velocity distribuion of actual members (see, e.g., figure 10 of White et al. 2010). Hence we adopt a figure of 30 per cent for each cluster's mass uncertainty arising from interlopers in the member sample. Note that we automatically account for the velocity bias, $b_{\rm v}$, by adopting a scaling relation based on simulated galaxies rather than dark matter particles (see Section 3.4 for further discussion).

The velocity dispersion measurements were obtained for a pre-selected set of clusters, and the sample was not further refined based on these measurements. So although the measurements are affected by noise and intrinsic scatter, we can expect positive and negative noise and scatter excursions to be equally likely. The dynamical mass measurements on this sample are thus not affected by Eddington bias; this is discussed further in Appendix A. We therefore calculate dynamical masses by directly inverting Equation 1, which gives $\sigma(M)$, in order to obtain $M(\sigma)$. For this computation we take the uncertainty on σ to be normal, and report the mean and standard deviation of $M(\sigma)$ after propagating the full error distribution.[18] We note that this procedure can yield biased dynamical masses if velocity dispersion and SZ effect measurements are correlated for individual clusters (Evrard et al. 2014). In fact, we may expect some degree of correlation between any pair of observables for a given cluster, because the same large scale structure is affecting all cluster observables (White et al. 2010). We defer a proper treatment of correlations between observables to future work.

3.4 Dynamical mass estimates

The masses thus estimated are listed in Table 2, along with the redshifts, velocity dispersions, number of members used and r_{200}. We also list the radius at which our spectroscopic coverage ends, $r_{\rm max}$, and the initial velocity dispersion measured within $r_{\rm max}$. Below we summarize the corrections applied with respect to our analysis in

[18] The error distribution is normal in σ but not in $M \propto \sigma^{1/\alpha}$ (with $1/\alpha \approx 3$). Therefore the mean mass is not the cube of the central value of σ. This difference depends only on the measurement uncertainty and for our sample its median is 3 per cent, with a maximum of 16 per cent for ACT-CL J0206.2−0114.

Table 4. Individual cluster mass uncertainty budget, given as a fraction of cluster mass. Central values are the medians of the cluster distributions and uncertainties are 16th and 84th percentiles; upper limits are 84th percentiles. The median is equal to zero for all values with upper limits. "Reported" uncertainties correspond to those in Table 2, which arise from the combination of the three effects preceding them, while "total" uncertainties include the 30 per cent scatter from the $\sigma - M$ scaling relation, which is fixed for all clusters, added in quadrature. The 15 per cent uncertainty in the velocity bias is an overall uncertainty on the average masses.

Source	Equator	South	All
Statistical	$0.31^{+0.21}_{-0.08}$	$0.25^{+0.09}_{-0.03}$	$0.28^{+0.20}_{-0.06}$
Member selection	$0.14^{+0.18}_{-0.14}$	< 0.01	$0.04^{+0.18}_{-0.04}$
Multidark correction	< 0.12	$0.07^{+0.18}_{-0.07}$	< 0.18
Reported	**0.36**	**0.26**	**0.31**
Scatter in $M(\sigma)$	0.30	0.30	0.30
Total	**0.47**	**0.40**	**0.44**
Velocity bias uncertainty	0.15	0.15	0.15

Sifón et al. (2013) and then present a detailed account of uncertainties entering our dynamical mass estimates, before comparing our mass estimates with masses derived from SZ measurements.

Two sources of bias are now accounted for that were not included in Sifón et al. (2013). The first is the radial coverage of spectroscopic members (which was discussed, but not corrected for, in Sifón et al. 2013) which includes (i) an iterative calculation of the velocity dispersion within r_{200} only for 24 clusters with $r_{\rm max} > r_{200}$ and (ii) a correction to the velocity dispersion, based on the velocity dispersion profile of subhaloes in the Multidark simulation (see Figure 4), for 20 clusters with $r_{\rm max} < r_{200}$. Over the full sample these two situations produce a net correction of −5 per cent, compared to applying no correction as in Sifón et al. (2013). The second source of bias is the relation between the velocity dispersion of dark matter particles and that of galaxies. We account for this difference by using the $\sigma - M$ scaling relation of galaxies derived by Munari et al. (2013), which gives average masses 20 per cent lower than those derived from the scaling relation of Evrard et al. (2008) used in Sifón et al. (2013). In addition, we have updated the minimum bin size in our member selection algorithm (cf. Section 3.1), which lowers the masses by an average 6 per cent with respect to the value adopted in Sifón et al. (2013). Because of these updates to our analysis, for the southern clusters we report masses that are, on average, (71 ± 8) per cent of those reported in Sifón et al. (2013).

We present a breakdown of the contributions to individual cluster mass uncertainties for the equatorial and southern samples in Table 4. The uncertainty budget is dominated by the scatter induced by interlopers. Based on the discussion presented in Section 3.3, we estimate that this uncertainty amounts roughly to 30 per cent in mass. Because this contribution corresponds to a constant uncertainty for all clusters, we do not include them in the uncertainties reported in Table 2. We do recommend this 30 per cent systematic (i.e., that cannot be reduced by observing more galaxies) uncertainty to be added to the reported uncertainties in any cosmological analysis that uses these dynamical masses, and we include it in our calculation of the SZ mass bias in Section 3.5. Similarly, based on the discussion in Section 1, we adopt a 15 per cent systematic uncertainty arising from the unknown velocity bias (5 per cent in velocity; e.g., Wu et al. 2013). This 15 per cent essentially accounts for i) the fact that our galaxy sample may not correspond to the galaxy samples used by Munari et al. (2013) to arrive at Equation 1 (because the velocity bias is luminosity-dependent), and ii) differences in scaling relations compared to that of Munari et al. (2013) that may arise because of different hydrodynamical implementations (each producing a different velocity bias). The unknown velocity bias therefore limits our constraints on the SZ mass bias (see Section 3.5).

Statistical uncertainties are the dominant contribution to the reported uncertainties, with a median contribution of 28 per cent of the cluster mass. Uncertainties from member selection and the scatter in the correction of Table 3 are subdominant. We note here that by "member selection" we mean uncertainties arising from including or rejecting particular galaxies through the shifting gapper. The true uncertainty from contaminating galaxies is included in the scaling relation scatter as discussed in Section 3.3. We make this distinction because there is a fraction of false members which cannot be identified observationally via their peculiar velocities (e.g., Mamon et al. 2010; White et al. 2010; Saro et al. 2013). For the SZ-selected clusters of the South Pole Telescope survey, Ruel et al. (2014) found that the uncertainty from member selection, estimated by "pseudo-observing" their stacked cluster, depends on the number of galaxies observed. For the number of members we observed (which is roughly a factor two larger than the average number of members observed by Ruel et al. 2014), their estimate of the combined statistical and member selection uncertainty is consistent with ours.

3.5 Comparison to SZ-derived masses

The usefulness of clusters for constraining cosmological parameters depends on the accurate calibration of the cluster mass scale. Calibrated SZ masses are especially informative because SZ surveys yield large samples of clusters reaching to high redshifts. While our dynamical and SZ mass proxies may have non-trivial mass or redshift-dependence, the data in our study permit us to constrain the average bias between these proxies within the mass range probed in this study.

We compare the dynamical masses to the SZ-derived masses, $M^{\rm SZ}_{500}$, in Figure 6. For the purpose of this comparison we rescale dynamical masses to M_{500} using the mass-concentration relation of Dutton & Macciò (2014). The SZ-derived masses assume a scaling relation between the SZ effect (specifically, Y_{500}) and mass based on the pressure profile of Arnaud et al. (2010), derived from X-ray observations of local ($z < 0.2$) clusters, and have been corrected for Eddington bias as detailed in Hasselfield et al. (2013), assuming a 20 per cent intrinsic scatter in Y_{500} at fixed true mass (the "UPP" masses of Hasselfield et al. 2013). We refrain from fitting a scaling relation to these data since this requires a proper calibration of the survey selection effects and accounting for the mass function and cosmological parameters; the dynamical mass–SZ scaling relation and inferred cosmological parameters will be presented in a future paper.

Beyond the assumptions used to obtain the SZ masses, any additional bias in the inferred mass relative to the true cluster mass is often parametrized in terms of the SZ mass bias, $1 - b_{\rm SZ}$ (e.g., Planck Collaboration 2015a), defined by the relation $\langle M_{\rm SZ}|M_{\rm true}\rangle = (1 - b_{\rm SZ})M_{\rm true}$. An understanding of this calibration is essential to the cosmological interpretation of cluster counts from SZ surveys. Similarly, our dynamical masses may be biased proxies for the true cluster mass. Following Hasselfield et al. (2013), we parametrize this bias with $\beta_{\rm dyn}$, defined by $\langle M_{\rm dyn}|M_{\rm true}\rangle \equiv \beta_{\rm dyn} M_{\rm true}$. For the re-

mainder of this section we use the word "bias" to refer to systematic effects on the sample, such as "Eddington bias," that do not average down to an expectation value of zero with an increasing sample size.

The SZ and dynamical mass data permit us to place limits on the ratio $(1 - b_{\rm SZ})/\beta_{\rm dyn}$ by comparing the average SZ and dynamical masses of the clusters from the cosmological sample. We first combine the dynamical masses into a single characteristic mass

$$\bar{M}_{\rm dyn} \equiv \frac{\sum_i w_i M_{i,\rm dyn}}{\sum_i w_i}, \tag{2}$$

where the $M_{i,\rm dyn}$ represent the individual dynamical mass measurements, and the w_i are weighting factors. For this analysis we set all $w_i = 1$, but see below for further discussion of the choice of weights. We also compute the error, through standard error analysis.[19] For the SZ masses, we form the analagous sum, $\bar{M}_{\rm SZ} \equiv (\sum_i w_i M_{i,\rm SZ})/(\sum_i w_i)$. Note that the weights w_i used in this expression are the same weights used to compute $\bar{M}_{\rm dyn}$; this is essential to obtaining an unbiased answer when we later combine the two characteristic masses.

Each mass measurement is contaminated by intrinsic scatter and noise, in the sense that

$$\bar{M}_{i,\rm dyn} = M_{i,\rm true} e^{\xi_i} + \delta M_i, \tag{3}$$

where $\delta M_{i,\rm true} \sim \mathcal{N}(0, \epsilon_i)$ is the contribution from measurement noise, and $\xi_i \sim \mathcal{N}(0, 0.3)$ is the contribution from intrinsic scatter. The expectation value for δM_i is zero, while the expectation value of e^{ξ_i} is 1.046. So when we combine our measurements into a characteristic mass we expect that

$$\langle \bar{M}_{\rm dyn} \rangle = \frac{\sum_i w_i \langle M_{i,\rm dyn} \rangle}{\sum_i w_i} = 1.046 \beta_{\rm dyn} \frac{\sum_i w_i M_{i,\rm true}}{\sum_i w_i}. \tag{4}$$

For the combination of the SZ masses, the expectation value is $\langle \bar{M}_{\rm SZ} \rangle = 1 - b_{\rm SZ}$, because the skewness introduced by intrinsic scatter has already been fully accounted for in the calculation of the $M_{\rm SZ}$ values used here by Hasselfield et al. (2013). Taking the ratio of these two characteristic masses gives

$$\frac{\langle \bar{M}_{\rm SZ} \rangle}{\langle \bar{M}_{\rm dyn} \rangle} = \frac{(1 - b_{\rm SZ})}{1.046 \beta_{\rm dyn}}. \tag{5}$$

Our measured values of $\bar{M}_{\rm SZ}$ and $\bar{M}_{\rm dyn}$ thus provide a useful meaurement of $(1 - b_{\rm SZ})/\beta_{\rm dyn}$. (We show in Appendix A that this ratio is unbiased.) For the 21 clusters in the cosmological sample, the characteristic dynamical mass under uniform weights is $\bar{M}_{\rm dyn} = (4.8 \pm 0.5) \times 10^{14} {\rm M}_\odot$, and the characteristic SZ mass is $\bar{M}_{\rm SZ} = (5.0 \pm 0.2) \times 10^{14} {\rm M}_\odot$. The ratio of calibration factors is then

$$\frac{(1 - b_{\rm SZ})}{\beta_{\rm dyn}} = 1.10 \pm 0.13\,({\rm stat.}) \pm 0.14\,({\rm syst.}) \tag{6}$$

where the 0.14 systematic uncertainty arises from the 15 per cent fractional uncertainty on the average dynamical masses due to the unknown velocity bias discussed in Section 3.4. We note again that, in computing Equation 6, we have accounted for the 30 per cent scatter in the $M(\sigma)$ relation (see Section 3.3) which is not included in the cluster mass uncertainties reported in Table 2 and shown in Figure 6. Recent estimates of the SZ mass bias combining weak lensing measurements and SZ mass estimates from Planck Collaboration (2015c) have found $M_{\rm SZ}/M_{\rm WL} \approx 0.7$ (von der Linden et al. 2014b; Hoekstra et al. 2015). These measurements were then used as priors for the cosmological analysis of Planck SZ-selected clusters (under the assumption that $\langle M_{\rm WL} \rangle = \langle M_{\rm true} \rangle$, Planck Collaboration 2015a), highlighting the importance of calibrating these biases. We note that both von der Linden et al. (2014b) and Hoekstra et al. (2015) probed higher masses than we do. In fact, both works found evidence (at 95 per cent confidence) for a mass-dependent bias which, at the typical masses of ACT clusters, is consistent with our estimate. Similar to us, Rines et al. (2016) found no evidence that the mass ratio $\langle \bar{M}_{\rm SZ} \rangle / \langle \bar{M}_{\rm dyn} \rangle$ is different from unity, using dynamical masses estimated with the caustic technique, in a mass regime similar to ours.

Battaglia et al. (2015) used a stacked weak lensing measurement on a subset of these clusters, which they fit using hydrodynamical simulations, and found an SZ mass bias $1 - b_{\rm SZ} = \bar{M}_{\rm SZ}/\bar{M}_{\rm WL} = 0.98 \pm 0.28$ (assuming $\langle M_{\rm WL} | M_{\rm true} \rangle = M_{\rm true}$, as has been assumed in recent studies). This value has been computed with weights that depend on the weak lensing measurements. As a consistency check, we estimate the average dynamical mass of the nine clusters used by Battaglia et al. (2015), using the same weak lensing weights, and find $\bar{M}_{\rm dyn-WL} = (4.7 \pm 1.4) \times 10^{14} {\rm M}_\odot$, which implies a mass ratio $\bar{M}_{\rm dyn-WL}/\bar{M}_{\rm WL} = 0.98 \pm 0.33$. Therefore the dynamical masses are consistent with the weak lensing masses derived by Battaglia et al. (2015).

We have used uniform weights $w_i = 1$ to obtain the ratio in Equation 6, but one might expect that more carefully chosen weights could provide a more precise answer. In fact the weights should be chosen with some care, as it is possible to introduce a bias into this ratio if one permits the weights to depend too much on the measured data themselves. For example, if we take weights $w_i = 1/\epsilon^2_{i,\rm dyn}$ (where $\epsilon_{i,\rm dyn}$ is the measurement uncertainty on the velocity dispersion of cluster i), we find that clusters with low dynamical mass are more strongly weighted, because the dynamical mass uncertainties are strongly correlated with the dynamical mass measurements. However, the SZ masses are limited by sample selection effects to lie above some minimum value, and the characteristic SZ mass under these weights is almost twice the characteristic dynamical mass. A somewhat weaker effect is that these weights (i.e., the w_i above) have the potential to introduce a sort of Eddington bias into the computation, even though we carefully constructed a sample for which the dynamical mass measurements were unbiased. By re-weighting the clusters in a way that is correlated with the dynamical mass measurements themselves, we are effectively subselecting for measurements that are more likely to have scattered below the true mass values.

To avoid such biases, one should not incorporate dynamical mass or its uncertainty into the weights. Similarly, one should be wary of using the measured SZ masses and uncertainties to set the weights. In the present data, using weights $w_i = 1/\epsilon^2_{i,\rm SZ}$ or $w_i = M^2_{i,\rm SZ}/\epsilon^2_{i,\rm SZ}$ changes the resulting ratio by +3 or -2 per cent, respectively, without reducing the uncertainty. We discuss alternative weighting schemes in Appendix A.

3.6 Cluster substructure

Probes of substructure within a galaxy cluster provide information on a cluster's dynamical state: for example, whether or not a recent merger event has occurred. Since the thermodynamic properties of clusters vary depending on their dynamical state, a measurement of the amount of substructure provides an important additional cluster property. Of particular interest to SZ experiments is how the integrated Y parameter fluctuates with dynamical state. Simulations have shown that Y can fluctuate by tens of percent shortly after

[19] The error in $\bar{M}$ is $(\sum_i w_i^2 \epsilon_i^2)^{1/2}/(\sum_i w_i)$, where ϵ_i is the error in M_i.

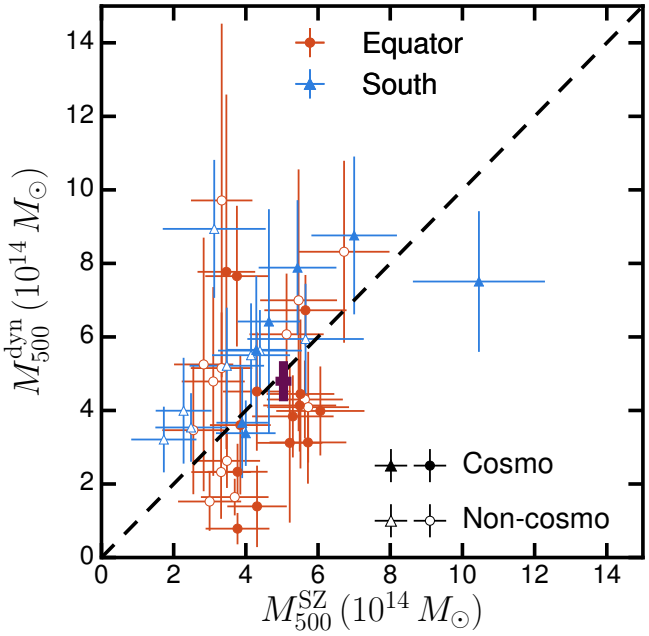

Figure 6. Comparison of dynamical and SZ-derived masses. Red circles and blue triangles show clusters in the equatorial and southern samples, respectively. Uncertainties on dynamical masses correspond to those reported in Table 2, and for clarity do not include the 30 per cent scatter in the $M(\sigma)$ relation. The dashed line shows equality and the purple cross shows the average SZ and dynamical masses of the combined southern and equatorial cosmological samples (filled symbols), calculated including the 30 per cent intrinsic scatter in the $M(\sigma)$ relation on the dynamical masses. There is an additional 15 per cent overall uncertainty on dynamical masses arising from the unknown galaxy velocity bias. See Section 3.5 for details.

merger events (e.g., Poole et al. 2007; Wik et al. 2008; Krause et al. 2012; Nelson et al. 2012), and that the intrinsic scatter of the $Y-M$ scaling relation for a subsample of relaxed clusters is smaller than for the entire sample (e.g., Battaglia et al. 2012; Yu et al. 2015). The latter conclusion was also reached by Sifón et al. (2013), albeit with low statistical significance.

Because of the sparser spectroscopic sampling used for the equatorial clusters, it is more difficult to identify localized substructure than it is with our dense sampling of the southern clusters (which is, however, confined to a smaller region of the cluster). We therefore refrain from a detailed, cluster-by-cluster analysis of substructure in the equatorial sample as we did for the southern clusters in Sifón et al. (2013). However, it is still valuable to study the presence of substructure in the sample as a whole, to be able to compare between our equatorial and southern samples, and whether the SZ selects different cluster populations than other techniques.

We use two quantities used by Sifón et al. (2013) to study cluster substructure. The first is the peculiar velocity of the BCG, $v_{\rm BCG} = c(z_{\rm BCG} - z_{\rm cl})/(1+z_{\rm cl})$, where $z_{\rm cl}$ is the cluster redshift listed in Table 2. Based on the results of Section 2.6, we assume an error of $100\,{\rm km\,s^{-1}}$ on $v_{\rm BCG}$. The second estimator we use is the DS test (Dressler & Shectman 1988), which measures the deviation of the velocity distribution in localized regions of a cluster with respect to the cluster as a whole through the statistic $\Delta = \sum_i \delta_i$, where

$$\delta^2 = \frac{N_{\rm local}}{\sigma^2}\left[(\bar{v}_{\rm local}-\bar{v})^2 + (\sigma_{\rm local}-\sigma)^2\right]^2 \qquad (7)$$

is calculated for each galaxy, where $\bar{v}_{\rm local}$ and $\sigma_{\rm local}$ are the mean and dispersion of the velocity distribution of the $N_{\rm local}$ nearest neighbors, where typically $N_{\rm local} = \sqrt{N_{200}}$. For each cluster we compare Δ to 1000 realizations where we shuffle the galaxy velocities, keeping their positions fixed. $\mathcal{S}_\Delta$ is then the probabilitiy to exceed the Δ measured for the clusters, given statistical fluctuations as determined through these realizations. We calculate 68 per cent level uncertainties on $\mathcal{S}_\Delta$ by varying $N_{\rm local}$ in the range $\sqrt{N_{200}} - 3 \leqslant N_{\rm local} \leqslant \sqrt{N_{200}} + 3$. Typically, $\mathcal{S}_\Delta < 0.05$ is taken as evidence for substructure (Pinkney et al. 1996). See Sifón et al. (2013) for more details.

We compare in Figure 7 the distributions of (absolute values of) BCG peculiar velocities, $|v_{\rm BCG}|$, and $\mathcal{S}_\Delta$ to those found in the Multidark simulation. In general, the southern sample shows more evidence of substructure than the equatorial sample through the DS test, with 38 per cent and 22 per cent, respectively, having $\mathcal{S}_\Delta < 0.05$. In turn, 31 per cent of Multidark clusters fulfill this criterion. Two-sided Kolmogorov-Smirnov tests, however, show no evidence of the distributions of either $\mathcal{S}_\Delta$ or $|v_{\rm BCG}|$ being different between the southern, equatorial and Multidark samples (all p-values from the KS tests are $\gtrsim 0.20$). In Sifón et al. (2013), we selected clusters as non-relaxed (i.e., containing substructure) if, among other properties, they had $|v_{\rm BCG}| > 0$ at 95 per cent confidence. In the southern sample 50 per cent of clusters pass this test, while 41 per cent (11/27) of the clusters in the equatorial sample do. This 40–50 per cent rate of non-relaxed clusters is somewhat lower than fractions found for X-ray– and optically–selected clusters (e.g., Böhringer et al. 2010; Wen & Han 2013). Using mock cluster observations, Lin et al. (2015) showed that the SZ significance can be boosted by up to 10 per cent for cool core (i.e., relaxed) clusters depending on the redshift, cuspiness and size of the cluster. This would then lead to a preferential selection of relaxed clusters, qualitatively consistent with our results. The fact that this bias is not apparent when comparing to Multidark clusters may relate to the fact that Multidark is a dark matter only simulation, but a detailed comparison is beyond the scope of this work.

3.7 The impact of centring on the BCG

As mentioned in Section 3.1, we have assumed that the BCGs correspond to the centre of the cluster potential. In this section we estimate the impact of this assumption on the reported masses.

We first re-calculate the velocity dispersions for all clusters assuming that the cluster centre is the centre of light instead of the BCG. To estimate the centre of light we take the luminosity-weighted average position of photometric members using photometric redshifts estimated by Menanteau et al. (2013) using the Bayesian Photometric Redshift (BPZ) code (Benítez 2000). The average mass ratio is $\langle M_{\rm CoL}/M_{\rm BCG}\rangle = 1.01 \pm 0.09$ with a standard deviation of 0.16, which is within the quoted mass uncertainties. Note that Viola et al. (2015) have shown, using weak lensing measurements, that the centre of light is generally significantly offset from the true cluster centre while BCGs are, on average, consistent with being at the centre of the cluster potential.

We also looked for clusters whose BCG cannot be identified unambiguously because there are other similarly bright member galaxies. Three southern (ACT-CL J0215−5212, ACT-CL J0232−5257 and ACT-CL J0521−5104) and four equatorial (ACT-CL J0239.8−0134, ACT-CL J0256.5+0006, ACT-CL J2055.4+0105 and ACT-CL J2302.5+0002) clusters fall under this category (see Menanteau et al. 2010, 2013, for optical images of ACT clusters; Section 4 for more detailed comments on some of these clusters). We estimate the masses of these clusters once more, taking the next most probable BCG candidate (where this is deter-

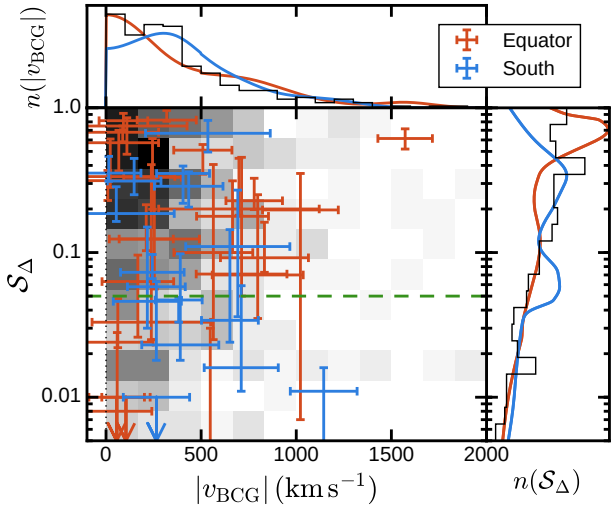

Figure 7. Comparison between BCG peculiar velocity and DS test significance level for the southern (blue) and equatorial (red) samples, and haloes in the Multidark simulation (grey scale background, where zero is white and one is black, and black histograms). The green, dashed horizontal line shows the threshold $\mathcal{S}_\Delta = 0.05$, below which the DS test is usually considered to provide evidence for substructure. The *top* and *right* panels show the corresponding histogram for the Multidark simulation and the summed probability distribution functions for the southern (blue) and equatorial (red) clusters, normalized to subtend the same area as the histograms.

mined by visual inspection) as the cluster centre. In all cases the mass difference is well within the reported uncertainties.

From these two tests we conclude that uncertainties due to the choice of cluster centre are within the quoted errorbars and therefore cluster centring does not introduce any biases or additional uncertainties on our mass estimates.

4 NOTABLE CLUSTERS

In this section we describe some notable clusters in the equatorial sample in more detail. Similar notes on southern clusters can be found in Sifón et al. (2013). We first summarize ACT clusters that have been studied in detail elsewhere and then discuss individual clusters.

4.1 Previously studied ACT clusters

El Gordo (ACT-CL J0102−4915, $z = 0.87$, Menanteau et al. 2012) is probably the most massive cluster known at $z > 0.8$ (Jee et al. 2014). It is a merging system composed of two roughly equal-mass subclusters colliding approximately perpendicular to the line-of-sight (Zitrin et al. 2013; Jee et al. 2014), probably seen about 1 Gyr after core passage (Ng et al. 2015). It hosts the highest-redshift known radio relics and halo (Lindner et al. 2014). Its dynamical mass ($M_{200} = (1.13 \pm 0.29) \times 10^{15}\,{\rm M}_\odot$, cf. Table 2) is significantly smaller than the total mass estimated from weak lensing ($M_{200} = (2.84 \pm 0.51) \times 10^{15}\,{\rm M}_\odot$, Jee et al. 2014), but the former can be expected to be biased when such an extreme system is assumed to be composed of a single component (as is the case here for consistency with the rest of the sample). As a result of the major merger, the total stellar mass in El Gordo is lower than the expectation based on its SZ effect (Hilton et al. 2013).

ACT-CL J0022.2−0036 ($z = 0.81$) is the highest-significance detection in the S82 sample (Hasselfield et al. 2013). The dynamical mass is consistent with independent mass estimates from weak lensing (Miyatake et al. 2013), optical richness and high-resolution SZ measurements (Reese et al. 2012), giving an inverse-variance-weighted average mass of $M_{200} = (7.8 \pm 0.9) \times 10^{14}{\rm M}_\odot$ (see also the discussion in Menanteau et al. 2013).

ACT-CL J0256.5+0006 ($z = 0.36$) was studied in detail by Knowles et al. (2015). It is one of the lowest-mass systems known to host a giant radio halo, which is likely produced by the interaction of two systems with a mass ratio of approximately 2:1 being observed prior to the first core crossing. The merging scenario is supported by the velocity distribution (ACT-CL J0256.5+0006 has $\mathcal{S}_\Delta < 0.01$ at 68 per cent confidence) and X-ray observations; there are two X-ray peaks coincident with two dominant galaxies. The velocity dispersions of the two components suggests that the reported mass, which assumes a single component, may be biased high by roughly 40 per cent, an amount comparable to the quoted uncertainty.

ACT-CL J0320.4+0032 ($z = 0.385$) is one of the few clusters whose BCG is known to host a type II quasar (Kirk et al. 2015). The low number of observed members precludes a detailed analysis of the cluster structure, but we note that a maximally-predictive histogram (Knuth 2006) of the galaxy velocities shows two peaks and a somewhat asymmetric distribution (see Figure B2), which suggests that ACT-CL J0320.4+0032 is a dynamically young cluster.

4.2 ACT-CL J0218.2−0041

ACT-CL J0218.2−0041 ($z = 0.673$) is one of the lowest-mass clusters in the sample (Table 2). In addition to the cluster itself, we have identified in our spectroscopic data an overdensity of eight galaxies at $z = 0.82$. Their velocity dispersion, while not necessarily representative of this system's velocity dispersion, is $\sigma_{\rm gal} = 880\,{\rm km\,s^{-1}}$, which would suggest a mass $M > 10^{14}{\rm M}_\odot$. We additionally identified a structure of 12 galaxies around $z = 0.73$ which, although it only spans $6000\,{\rm km\,s^{-1}}$, has $\sigma_{\rm gal} = 2320\,{\rm km\,s^{-1}}$, suggesting that the structure is probably not collapsed.

Two of the three structures have velocity dispersions that suggest cluster-sized systems. The fact that we detect these overdensities, instead of non-members being scattered in redshift space, suggests that ACT-CL J0218.2−0041 may be associated with a larger cosmic structure along the line of sight, with two relatively massive clusters at $z = 0.67$ and $z = 0.82$ possibly connected by a filament (the $z = 0.73$ structure). For comparison, we also detected additional galaxy overdensities in the lines of sight of ACT-CL J0235−5121 (7 galaxies at $z = 0.44$) and ACT-CL J0215.4+0030 (8 galaxies at $z = 0.39$), which have $\sigma_{\rm gal} = 280\,{\rm km\,s^{-1}}$ and $\sigma_{\rm gal} = 170\,{\rm km\,s^{-1}}$, respectively. This shows that low-mass groups may in fact be identified with our observations—that is, the structures detected behind ACT-CL J0218.2−0041 are not likely to be low mass groups. This large-scale scenario is also appealing given the low mass of ACT-CL J0218.2−0041. It would be interesting to explore the impact of this structure on the measured SZ effect, and similarly on X-ray emission, but this is deferred to future work.

4.3 ACT-CL J0326.8−0043

ACT-CL J0326.8−0043 ($z = 0.447$) was first discovered as part of the Massive Cluster Survey (MACS J0326.8−0043, Ebeling et al.

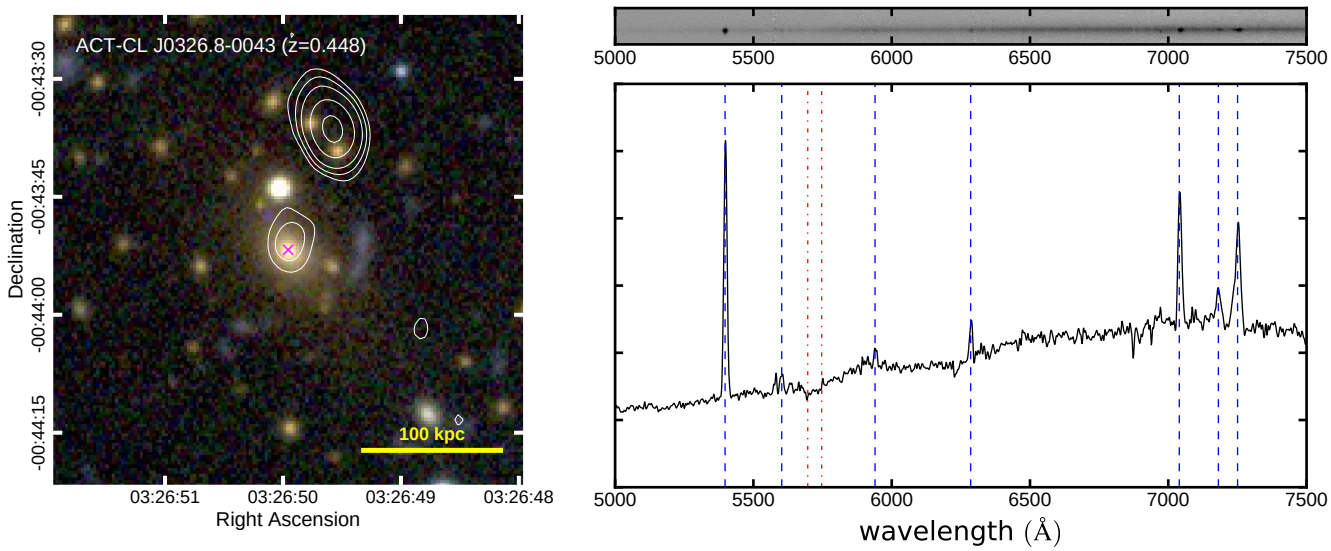

Figure 8. The BCG of ACT-CL J0326.8−0043 at $z = 0.45$. *Left:* Optical *gri* image from SDSS with 1.4 GHz contours from the FIRST survey overlaid in white and shown at $(3, 5, 8, 15, 25)\sigma$ levels, where $\sigma = 0.14\,\mathrm{mJy\,beam^{-1}}$. The BCG is marked with a magenta cross and the thick yellow line in the bottom-right corner is 100 kpc wide, corresponding to 17.″4 at the cluster redshift. North is up and East is left. *Right:* Optical one- (bottom) and two-dimensional (top) Gemini/GMOS spectra. The former is smoothed with a 3-pixel boxcar. In the bottom panel, detected emission lines are marked with dashed blue lines (in order of increasing wavelength: [O II], Ne III, Hδ, Hγ, Hβ and [O III]$\lambda\lambda$4959, 5007); the Ca II K,H absorption doublet is marked with dash-dotted red lines. The asymmetric broadening of the [O III]λ5007 line is an artifact introduced by interpolating the GMOS chip gaps. The vertical axis is in arbitrary units.

2001). The left panel of Figure 8 shows a SDSS *gri* image of the centre of the cluster, with 1.4 GHz contours from the Faint Images of the Radio Sky at Twenty centimetres (FIRST, Becker et al. 1995) survey overlaid in white. The BCG (which we refer to simply as J0326 in the remainder of this section) shows strong emission lines across the optical spectrum (Figure 8, right panel). Because our Gemini/GMOS spectrum is not flux-calibrated we use the line measurements from the SDSS MPA/JHU Value-Added Galaxy Catalog (Brinchmann et al. 2004) throughout. We cannot distinguish whether the emission in J0326 is dominated by star formation or an AGN from the line ratio diagnostic introduced by Lamareille (2010), appropriate for high-redshift ($z > 0.4$) objects for which Hα falls outside the optical wavelength range (specifically, $\log([\mathrm{O\,II}]\lambda\lambda3726 + 3729/\mathrm{H}\beta) = 0.57 \pm 0.03$ and $\log([\mathrm{O\,III}]\lambda5007/\mathrm{H}\beta) = -0.23 \pm 0.03$).

The left panel of Figure 8 shows that there is additionally significant 1.4 GHz emission from a point source whose peak is offset 1.″2 (7 kpc) from the BCG (but note that the positional uncertainty in the FIRST source is $\approx 1''$), but again the nature of the emission cannot be determined. In the case of star forming galaxies with no AGN contamination, the 1.4 GHz luminosity can be used as an unobscured tracer of star formation. The 1.4 GHz luminosity of the source associated to the BCG is $\log L_{1.4}/(\mathrm{W\,Hz^{-1}}) = 24.0$, which at face value implies a star formation rate (SFR) of several hundred $\mathrm{M_\odot\,yr^{-1}}$ (Hopkins et al. 2003). In contrast, the [O II]λ3727 doublet suggests a SFR of a few tens of $\mathrm{M_\odot\,yr^{-1}}$. Systems with such marked differences in estimated SFRs are almost always AGN hosts (J. Brinchmann, private communication). Chang et al. (2015) fitted spectral energy distributions to optical SDSS data plus mid infrared data from the Wide-field Infrared Survey Explorer (WISE, Wright et al. 2010) of one million objects. For J0326 they estimated a best-fit star formation rate of $\mathrm{SFR} = 15^{+10}_{-5}\,\mathrm{M_\odot\,yr^{-1}}$, consistent with the radio emission being dominated by nuclear activity. If this is the case then J0326 is a new Type II AGN BCG (Type I AGNs are characterized by broad components in the [O III] lines), similar to the case of the BCG of ACT-CL J0320.4+0032 recently reported by Kirk et al. (2015) and noted in Section 4.1. Therefore J0326 probably adds to the very sparse sample of Type II AGNs in BCGs (see references in Kirk et al. 2015).

Gilmour et al. (2009) analyzed a 10 ks *Chandra* observation of ACT-CL J0326.8−0043 and found no evidence for an X-ray point source in the BCG location to suggest the presence of an AGN; however, the observations are too shallow to draw any firm conclusions. While available X-ray data are not sufficient to establish the cooling rate in the cluster core, all evidence points to a fairly relaxed cluster. There is no evidence for substructure from the velocity distribution; $v_{\mathrm{BCG}} = 205 \pm 147\,\mathrm{km\,s^{-1}}$ suggests the BCG is located at the centre of the potential; and the magnitude gap to the second-brightest member (based on photometric redshifts to avoid a bias due to spectroscopic incompleteness) is relatively large, $\Delta m_{12} = 1.62$, which is also an indication of a dynamically old cluster (e.g., Wen & Han 2013).

4.4 ACT-CL 2050.5−0055

The BCG of ACT-CL 2050.5−0055 ($z = 0.623$; hereafter simply "the BCG") has the highest peculiar velocity of all BCGs in the ACT sample. In fact, the BCG is rejected by our member selection algorithm, with a peculiar velocity of $v_{\mathrm{BCG}} = -(1572 \pm 143)\,\mathrm{km\,s^{-1}}$, different from zero at 11σ, compared with a cluster velocity dispersion $\sigma_{200} = (511 \pm 97)\,\mathrm{km\,s^{-1}}$, the lowest σ_{200} in the entire sample (cf. Table 2). The BCG also has a redshift in the SDSS catalogue, $z_{\mathrm{SDSS}} = 0.6133 \pm 0.0002$, which would make v_{BCG} more negative by about $200\,\mathrm{km\,s^{-1}}$ (compared to $z_{\mathrm{Gemini}} = 0.6141 \pm 0.0003$). For the purpose of this discussion, this difference is not important and we will continue to use z_{Gemini} throughout. Such a high v_{BCG} probably originated as a result of either merging activity or strong galaxy-galaxy interactions in the centre (Martel et al. 2014). Re-

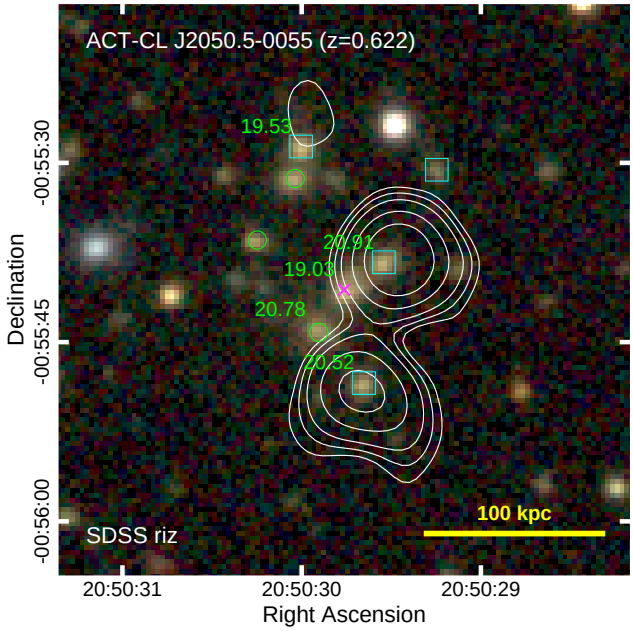

Figure 9. Optical *riz* image of the central region of ACT-CL J2050.5−0055 ($z = 0.62$) from SDSS, with 1.4 GHz contours from the FIRST survey overlaid in white at $(3, 5, 8, 15, 25)\sigma$ levels, where $\sigma = 0.15\,\mathrm{mJy\,beam^{-1}}$. The BCG is marked with a magenta cross; cyan squares show other spectroscopically confirmed cluster members and green circles show bright photometric redshift members. Greeen numbers to the top-left of the five brightest cluster members correspond to dereddened *i*-band magnitudes from SDSS. The thick yellow line in the bottom-right corner is 100 kpc wide, corresponding to 14.″7 at the cluster redshift. North is up and East is left.

garding the possibility of a cluster-scale merger, the DS test does not reveal any evidence for substructure, although we do not have enough member galaxies to draw firm conclusions. As seen in Figure 7, there are haloes in our Multidark sample that have comparable BCG velocities but they tend to have lower values of $\mathcal{S}_\Delta$ than ACT-CL 2050.5−0055.

Coziol et al. (2009) studied a sample of 452 BCGs in low-redshift clusters, and found that BCGs have, on average, $|v_{\rm BCG}| = 0.32\sigma$ (where σ is the cluster velocity dispersion), with only three BCGs having velocities $|v_{\rm BCG}| > 2\sigma$. In comparison, the BCG of ACT-CL 2050.5−0055 has $v_{\rm BCG} = -(3.1 \pm 0.7)\,\sigma_{200}$.[20] Similarly, all the BCGs studied by Coziol et al. (2009) have $|v_{\rm BCG}| < 1500\,\mathrm{km\,s^{-1}}$. Therefore the BCG of ACT-CL 2050.5−0055 is unique in this respect; it will be interesting to study the conditions that led to such high $|v_{\rm BCG}|$. All other spectroscopic members in the cluster centre (Figure 9) have peculiar velocities between −550 and 350 $\mathrm{km\,s^{-1}}$, consistent with the low cluster velocity dispersion.

Figure 9 shows FIRST contours overlaid on an SDSS *gri* image of the central region of ACT-CL 2050.5−0055. There are two point-like sources coinciding with two galaxies within 100 kpc from the BCG. The integrated 1.4 GHz luminosities of the northern and southern sources are $\log L_{1.4}/(\mathrm{W\,Hz^{-1}}) = 25.1$ and 25.0, respectively. Such high luminosities suggest that indeed these are point sources rather than extended emission originating in the ICM.

[20] Including the BCG in the member sample by hand increases the cluster velocity dispersion to $\sigma_{200} = (607 \pm 107)\,\mathrm{km\,s^{-1}}$, yielding $v_{\rm BCG} = -(2.6 \pm 0.5)\,\sigma_{200}$.

All spectroscopic members shown in Figure 9 have spectra typical of passive, elliptical galaxies with no signs of activity, with strong Ca II K,H absorption and no optical emission lines.

We also show in Figure 9 the deredenned *i*-band magnitudes from the SDSS catalog for the five brightest galaxies (spectroscopic and photometric members). The BCG is brighter than any other galaxy by 0.5 mag. In combination with its central location relative to the galaxy distribution, it is unlikely that the BCG is not the central galaxy of the cluster. In particular, the galaxies that coincide with radio sources are only the third and fifth brightest galaxies, making it unlikely that any of them is the central galaxy. We conclude that misidentification of the central galaxy is unlikely to explain the high $|v_{\rm BCG}|$ reported for this cluster.

4.5 ACT-CL J2055.4+0105

As mentioned in Section 3.7, the identification of the BCG is not obvious for this cluster at $z = 0.409$. In fact, we identify four galaxies along a straight line extending 1.2 Mpc SE of the BCG (the BCG is the one further NW of the four), the faintest of which is only 0.86 mag fainter than the BCG (all four galaxies are spectroscopically confirmed). Two of the four galaxies (the first and third brightest, and in the NW-SE line joining them, which are separated by 940 kpc) have extended light envelopes characteristic of cD galaxies. Only the fiducial BCG is clearly surrounded by a large overdensity of red galaxies, suggesting it is indeed the central galaxy. The fact that its peculiar velocity is consistent with zero also supports this scenario. The "alternative BCG" velocity (of $-700\,\mathrm{km\,s^{-1}}$) shown in Figure B2 corresponds to this secondary cD galaxy; the other two galaxies have peculiar velocities of less than 400 $\mathrm{km\,s^{-1}}$.

Overall, this elongated configuration with multiple dominant galaxies strongly suggests that ACT-CL J2055.4+0105 is undergoing a major merger between at least two massive subclusters, and possibly more. The DS test does not reveal any evidence for substructure ($\mathcal{S}_\Delta = 0.81 \pm 0.10$), but we note that this is also the case for El Gordo (Sifón et al. 2013). This is because the DS test (nor, indeed, dynamical information in general) is not sensitive to mergers happening along the plane of the sky. As with other clusters described in this section, more data would be required for a detailed assessment of this system.

4.6 ACT-CL J2302.5+0002

ACT-CL J2302.5+0002 at $z = 0.520$ is also one of the lowest-mass clusters in the sample. We show the central 300 kpc of this cluster in Figure 10, which shows strong evidence that the brightest galaxy is not the *central* cluster galaxy: the second-brightest galaxy, 130 kpc away, shows strong 1.4 GHz emission and what appears to be a strongly lensed background galaxy around it. The coordinates given by Menanteau et al. (2013) indeed correspond to the brightest galaxy, but for our purposes we take the second-brightest galaxy as the cluster centre. ACT-CL J2302.5+0005 is therefore the only cluster for which we do not take the brightest galaxy as the cluster centre in Section 3. As mentioned in Section 3.7, adopting either galaxy as the centre gives consistent mass estimates; using the brightest galaxy instead of the central one we obtain $M_{200} = (1.9 \pm 0.7) \times 10^{14}\mathrm{M_\odot}$, compared to the fiducial value of $M_{200} = (2.4 \pm 0.7) \times 10^{14}\mathrm{M_\odot}$. We do not detect any optical emission lines in either galaxy.

Although such clear examples of brightest galaxies not being the central galaxy are rare, the value of the separation between the two galaxis is not uncommon (Skibba et al. 2011; Martel

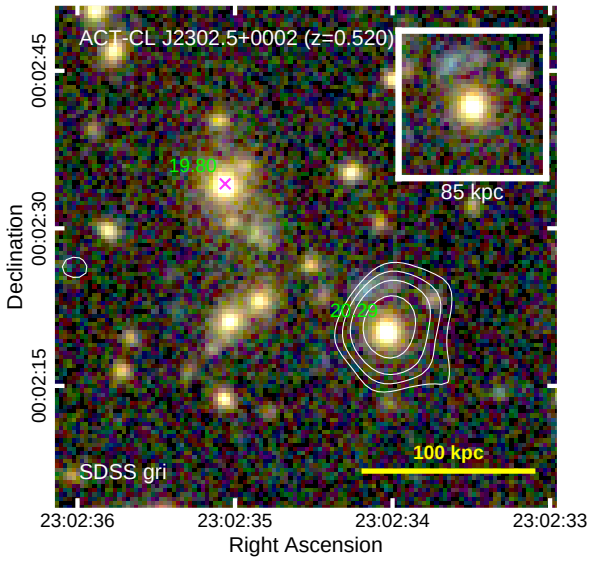

Figure 10. Optical SDSS *gri* image of the inner 300 kpc of ACT-CL J2302.5+0002. Symbols, labels and contours are as in Figure 9. The inset in the top-right corner is 85 kpc on a side and shows the region around the second-brightest galaxy without the radio contours, which show what appears to be a strongly lensed background image. The thick yellow line in the bottom-right corner is 100 kpc wide, corresponding to 16.″0 at the cluster redshift. North is up and East is left.

et al. 2014). Martel et al. (2014) have argued that the positional offset of the BCG is not as robust an indication of major mergers as the velocity offset, $v_{\rm BCG}/\sigma$, where σ is the cluster velocity dispersion. As shown in Figure B2, both galaxies have large peculiar velocities, with $v = -470\,{\rm km\,s^{-1}}$ ($v/\sigma_{200} = 0.70$) and $v = -600\,{\rm km\,s^{-1}}$ ($v/\sigma_{200} = 0.89$) for the central and brightest galaxies, respectively. Similar to (but less extreme than) the BCG in ACT-CL J2050.5−0055, these peculiar velocities—especially given the small cluster velocity dispersion—strongly suggest that ACT-CL J2302.5+0002 is undergoing a major merger (Martel et al. 2014), but the available data do not allow us to perform a more detailed analysis.

5 CONCLUSIONS

We have carried out a spectroscopic follow-up effort of ACT SZ-selected clusters in the equatorial survey in the redshift range $0.3 < z < 0.9$. Combined with our previous follow-up program of the southern clusters and archival data, we present velocity dispersions and dynamical masses for 44 clusters at $0.24 < z < 1.06$ with a median of 55 spectroscopic members per cluster.

We calibrate our velocity dispersion measurements using the Multidark simulation, taking into account the spectroscopic coverage of clusters which is qualitatively different for southern and equatorial clusters, owing to the different optical imaging available (namely, targeted $5' \times 5'$ observations in the south and full SDSS coverage in the equator, Figure 2). We find that velocity dispersions are unbiased so long as the measurement includes galaxies out to r_{200} but the azimuthal distribution of spectroscopic targets is not important for our purposes (see Section 3.2 and Figure 3). We use the average radial velocity dispersion profile of subhaloes in Multidark to correct measurements for clusters whose coverage does not reach r_{200} and include the uncertainties from this correction (Table 3) in the reported velocity dispersions.

We use a scaling relation between galaxy velocity dispersion and cluster mass derived from zoomed cosmological hydrodynamical simulations to infer dynamical masses consistently for the full sample of clusters with spectroscopic observations. We make a detailed assessment of the different contributions to the reported mass uncertainties, which are dominated by a ≈30 per cent scatter in the scaling relation induced by interlopers, triaxiality and the intrinsic scatter of the relation. Because this is a constant value, we do not include this contribution in the reported cluster mass uncertainties but recommend that it be included in cosmological analyses derived from these data. Statistical uncertainties from our average 55 members per cluster are comparable to said scatter, while uncertainties from member selection and the spectroscopic aperture selection are subdominant.

The updated dynamical mass estimates of the southern clusters are, on average, 71 per cent of the masses presented in Sifón et al. (2013). This overall difference results from (i) accounting for the observing strategies used to get the galaxy redshifts when calculating cluster velocity dispersions (Section 3.2), and (ii) using a $\sigma - M_{200}$ scaling relation that includes the effects of baryonic physics and dynamical friction (Section 3.3). We find that masses derived from the SZ effect assuming a scaling relation based on the pressure profile of Arnaud et al. (2010) are consistent with the dynamical masses and report a mass bias which results from the combination of the dynamical mass bias and the SZ bias, $(1 - b_{\rm SZ})/\beta_{\rm dyn} = \bar{M}^{\rm SZ}_{500}/\bar{M}^{\rm dyn}_{500} = 1.10 \pm 0.13$, with an additional 0.14 systematic uncertainty due to the unknown galaxy velocity bias (see Figure 6 and Section 3.5), consistent with previous estimates from the literature if one accounts for the different mass regimes. Hasselfield et al. (2013) used the dynamical masses of Sifón et al. (2013) as prior information on the cosmological analysis derived from the SZ cluster counts and found that dynamical masses suggested a higher σ_8 than other cosmological probes. The new, lower dynamical masses will bring the estimate of σ_8 down. A cosmological analysis incorporating these new dynamical mass estimates will be presented in a future paper.

We also highlight five newly-characterized clusters. ACT-CL J0218.2−0041 ($z = 0.67$) appears to be part of a structure where two cluster-sized systems are connected by a filament along the line of sight. The BCG of ACT-CL J0326.8−0043 ($z = 0.45$) is likely a rare Type II AGN host which also seems to be associated with strong radio emission. The BCG of ACT-CL 2050.5−0055 ($z = 0.62$) has a peculiar velocity of $v_{\rm BCG} = 3\sigma_{200}$ and is surrounded by double-peaked (probably point-source) radio emission. ACT-CL J2055.4+0105 ($z = 0.41$) has four bright, locally-dominant galaxies separated by 1.2 Mpc along a straight line. Finally, ACT-CL J2302.5+0002 ($z = 0.52$) is a clear example of the brightest galaxy not being the central cluster galaxy, confirmed by the presence of a strong lensing arc around the second-brightest galaxy. Further follow-up studies will reveal more details about these intriguing systems.

The uncertainty on the average dynamical mass is dominated by the scatter in the $\sigma - M$ relation (see Table 4), which cannot be significantly reduced by observing more galaxies per cluster. Ntampaka et al. (2015b) recently developed a machine learning approach to measure dynamical masses which incorporates information about the distribution of galaxies and their velocities to predict cluster masses, which has been successfully applied to mock observations that include the effects of impurity and incompleteness,

reducing the errors by up to 60 per cent (Ntampaka et al. 2015a). Further tests on more realistic galaxy catalogues will assess its effectiveness in measuring galaxy cluster masses in real observations.

ACKNOWLEDGMENTS

We thank Jarle Brinchmann for help interpreting the spectrum of the BCG of ACT-CL J0326.8−0043, Gary Mamon for useful discussions on cluster velocity dispersion profiles and Stefano Andreon and Bruce Partridge for useful comments during the preparation of this manuscript. We are grateful to the referee, August Evrard, for a thorough review of our work, which helped improve the clarity and robustness of the discussions presented in this paper.

C.S. acknowledges support from the European Research Council under FP7 grant number 279396 awarded to H. Hoekstra. N.B. and R.H. acknowledge support from the Spitzer Fellowship. L.F.B.'s research is supported by FONDECYT under project 1120676. A.K. acknowledges support from NSF grant 1312380.

This work was supported by the U.S. National Science Foundation through awards AST-0408698 and AST-0965625 for the ACT project, as well as awards PHY-0855887 and PHY-1214379. Funding was also provided by Princeton University, the University of Pennsylvania, and a Canada Foundation for Innovation (CFI) award to UBC. ACT operates in the Parque Astronómico Atacama in northern Chile under the auspices of the Comisión Nacional de Investigación Científica y Tecnológica de Chile (CONICYT). Computations were performed on the GPC supercomputer at the SciNet HPC Consortium. SciNet is funded by the CFI under the auspices of Compute Canada, the Government of Ontario, the Ontario Research Fund – Research Excellence; and the University of Toronto.

Based in part on observations obtained at the Gemini Observatory, which is operated by the Association of Universities for Research in Astronomy, Inc., under a cooperative agreement with the NSF on behalf of the Gemini partnership: the National Science Foundation (United States), the Science and Technology Facilities Council (United Kingdom), the National Research Council (Canada), CONICYT (Chile), the Australian Research Council (Australia), Ministério da Ciência e Tecnologia (Brazil) and Ministerio de Ciencia, Tecnología e Innovación Productiva (Argentina).

Funding for SDSS-III has been provided by the Alfred P. Sloan Foundation, the Participating Institutions, the National Science Foundation, and the U.S. Department of Energy Office of Science. The SDSS-III web site is http://www.sdss9.org/.

The MultiDark Database used in this paper and the web application providing online access to it were constructed as part of the activities of the German Astrophysical Virtual Observatory as result of a collaboration between the Leibniz-Institute for Astrophysics Potsdam (AIP) and the Spanish MultiDark Consolider Project CSD2009-00064. The Bolshoi and MultiDark simulations were run on the NASA's Pleiades supercomputer at the NASA Ames Research Center. The MultiDark-Planck (MDPL) and the BigMD simulation suite have been performed in the Supermuc supercomputer at LRZ using time granted by PRACE.

IRAF is distributed by the National Optical Astronomy Observatory, which is operated by the Association of Universities for Research in Astronomy (AURA) under a cooperative agreement with the National Science Foundation.

This work has made use of IPython (Prez & Granger 2007) and of the python packages numpy and scipy. Plots have been made using matplotlib (Hunter 2007).

REFERENCES

Afshordi N., 2008, ApJ, 686, 201
Aihara H., et al., 2011, ApJS, 193, 29
Alam S., et al., 2015, ApJS, 219, 12
Allen S. W., Evrard A. E., Mantz A. B., 2011, ARA&A, 49, 409
Andersson K., et al., 2011, ApJ, 738, 48
Andreon S., de Propris R., Puddu E., Giordano L., Quintana H., 2008, MNRAS, 383, 102
Annis J., et al., 2014, ApJ, 794, 120
Arnaud M., Pratt G. W., Piffaretti R., Böhringer H., Croston J. H., Pointecouteau E., 2010, A&A, 517, A92
Barrena R., Girardi M., Boschin W., Dasí M., 2009, A&A, 503, 357
Battaglia N., Bond J. R., Pfrommer C., Sievers J. L., 2012, ApJ, 758, 74
Battaglia N., et al., 2015, preprint, (arXiv:1509.08930)
Becker R. H., White R. L., Helfand D. J., 1995, ApJ, 450, 559
Beers T. C., Flynn K., Gebhardt K., 1990, AJ, 100, 32
Benítez N., 2000, ApJ, 536, 571
Benson B. A., et al., 2013, ApJ, 763, 147
Biviano A., Murante G., Borgani S., Diaferio A., Dolag K., Girardi M., 2006, A&A, 456, 23
Bocquet S., et al., 2015, ApJ, 799, 214
Böhringer H., et al., 2010, A&A, 514, A32
Bonamente M., Joy M., LaRoque S. J., Carlstrom J. E., Nagai D., Marrone D. P., 2008, ApJ, 675, 106
Boschin W., Girardi M., Barrena R., Biviano A., Feretti L., Ramella M., 2004, A&A, 416, 839
Brinchmann J., Charlot S., White S. D. M., Tremonti C., Kauffmann G., Heckman T., Brinkmann J., 2004, MNRAS, 351, 1151
Burgh E. B., Nordsieck K. H., Kobulnicky H. A., Williams T. B., O'Donoghue D., Smith M. P., Percival J. W., 2003, in Iye M., Moorwood A. F. M., eds, SPIEVol. 4841, Instrument Design and Performance for Optical/Infrared Ground-based Telescopes. pp 1463–1471, doi:10.1117/12.460312
Carlberg R. G., 1994, ApJ, 433, 468
Chang Y.-Y., van der Wel A., da Cunha E., Rix H.-W., 2015, ApJS, 219, 8
Colín P., Klypin A. A., Kravtsov A. V., 2000, ApJ, 539, 561
Coziol R., Andernach H., Caretta C. A., Alamo-Martínez K. A., Tago E., 2009, AJ, 137, 4795
Crawford S. M., et al., 2010, in Observatory Operations: Strategies, Processes, and Systems III. p. 773725, doi:10.1117/12.857000
Danese L., de Zotti G., di Tullio G., 1980, A&A, 82, 322
Dressler A., Shectman S. A., 1988, AJ, 95, 985
Dressler A., Smail I., Poggianti B. M., Butcher H., Couch W. J., Ellis R. S., Oemler Jr. A., 1999, ApJS, 122, 51
Dünner R., et al., 2013, ApJ, 762, 10
Dutton A. A., Macciò A. V., 2014, MNRAS, 441, 3359
Ebeling H., Edge A. C., Henry J. P., 2001, ApJ, 553, 668
Eddington A. S., 1913, MNRAS, 73, 359
Evrard A. E., 1989, ApJL, 341, L71
Evrard A. E., et al., 2008, ApJ, 672, 122
Evrard A. E., Arnault P., Huterer D., Farahi A., 2014, MNRAS, 441, 3562
Fadda D., Girardi M., Giuricin G., Mardirossian F., Mezzetti M., 1996, ApJ, 473, 670
Faltenbacher A., Diemand J., 2006, MNRAS, 369, 1698
Fowler J. W., et al., 2007, AppOpt, 46, 3444
Gifford D., Miller C., Kern N., 2013, ApJ, 773, 116
Gilmour R., Best P., Almaini O., 2009, MNRAS, 392, 1509
Girardi M., Giuricin G., Mardirossian F., Mezzetti M., Boschin W., 1998, ApJ, 505, 74
Gruen D., et al., 2014, MNRAS, 442, 1507
Guo H., et al., 2015a, MNRAS, 446, 578
Guo H., et al., 2015b, MNRAS, 453, 4368
Hasselfield M., et al., 2013, JCAP, 7, 008
High F. W., et al., 2010, ApJ, 723, 1736
Hilton M., et al., 2013, MNRAS, 435, 3469
Hoekstra H., Mahdavi A., Babul A., Bildfell C., 2012, MNRAS, 427, 1298

Hoekstra H., Herbonnet R., Muzzin A., Babul A., Mahdavi A., Viola M., Cacciato M., 2015, MNRAS, 449, 685
Hook I. M., Jørgensen I., Allington-Smith J. R., Davies R. L., Metcalfe N., Murowinski R. G., Crampton D., 2004, PASP, 116, 425
Hopkins A. M., et al., 2003, ApJ, 599, 971
Hunter J. D., 2007, Computing in Science & Engineering, 9
Jee M. J., Hughes J. P., Menanteau F., Sifón C., Mandelbaum R., Barrientos L. F., Infante L., Ng K. Y., 2014, ApJ, 785, 20
Kirk B., et al., 2015, MNRAS, 449, 4010
Klypin A., Holtzman J., 1997, ArXiv Astrophysics e-prints,
Knowles K., et al., 2015, preprint, (arXiv:1506.01547)
Knuth K. H., 2006, ArXiv Physics e-prints,
Krause E., Pierpaoli E., Dolag K., Borgani S., 2012, MNRAS, 419, 1766
Kurtz M. J., Mink D. J., 1998, PASP, 110, 934
Lamareille F., 2010, A&A, 509, A53
Lau E. T., Nagai D., Kravtsov A. V., 2010, ApJ, 708, 1419
Lin H. W., McDonald M., Benson B., Miller E., 2015, ApJ, 802, 34
Lindner R. R., et al., 2014, ApJ, 786, 49
Mahdavi A., Hoekstra H., Babul A., Bildfell C., Jeltema T., Henry J. P., 2013, ApJ, 767, 116
Mamon G. A., Biviano A., Murante G., 2010, A&A, 520, A30
Mantz A., Allen S. W., Rapetti D., Ebeling H., 2010, MNRAS, 406, 1759
Marriage T. A., et al., 2011a, ApJ, 731, 100
Marriage T. A., et al., 2011b, ApJ, 737, 61
Marrone D. P., et al., 2012, ApJ, 754, 119
Martel H., Robichaud F., Barai P., 2014, ApJ, 786, 79
Medezinski E., Broadhurst T., Umetsu K., Oguri M., Rephaeli Y., Benítez N., 2010, MNRAS, 405, 257
Menanteau F., et al., 2010, ApJ, 723, 1523
Menanteau F., et al., 2012, ApJ, 748, 7
Menanteau F., et al., 2013, ApJ, 765, 67
Miyatake H., et al., 2013, MNRAS, 429, 3627
Motl P. M., Hallman E. J., Burns J. O., Norman M. L., 2005, ApJL, 623, L63
Munari E., Biviano A., Borgani S., Murante G., Fabjan D., 2013, MNRAS, 430, 2638
Nagai D., 2006, ApJ, 650, 538
Nelson K., Rudd D. H., Shaw L., Nagai D., 2012, ApJ, 751, 121
Ng K. Y., Dawson W. A., Wittman D., Jee M. J., Hughes J. P., Menanteau F., Sifón C., 2015, MNRAS, 453, 1531
Ntampaka M., Trac H., Sutherland D. J., Fromenteau S., Poczos B., Schneider J., 2015a, preprint, (arXiv:1509.05409)
Ntampaka M., Trac H., Sutherland D. J., Battaglia N., Póczos B., Schneider J., 2015b, ApJ, 803, 50
Old L., Gray M. E., Pearce F. R., 2013, MNRAS, 434, 2606
Old L., et al., 2014, MNRAS, 441, 1513
Old L., et al., 2015, MNRAS, 449, 1897
Pacaud F., et al., 2007, MNRAS, 382, 1289
Pinkney J., Roettiger K., Burns J. O., Bird C. M., 1996, ApJS, 104, 1
Planck Collaboration 2011a, A&A, 536, A11
Planck Collaboration 2011b, A&A, 536, A12
Planck Collaboration 2013, A&A, 550, A129
Planck Collaboration 2014, A&A, 571, A16
Planck Collaboration 2015b, preprint, (arXiv:1502.01589)
Planck Collaboration 2015a, preprint, (arXiv:1502.01597)
Planck Collaboration 2015c, preprint, (arXiv:1502.01598)
Poole G. B., Babul A., McCarthy I. G., Fardal M. A., Bildfell C. J., Quinn T., Mahdavi A., 2007, MNRAS, 380, 437
Prada F., Klypin A. A., Cuesta A. J., Betancort-Rijo J. E., Primack J., 2012, MNRAS, 423, 3018
Prez F., Granger B. E., 2007, Computing in Science & Engineering, 9
Quintana H., Carrasco E. R., Reisenegger A., 2000, AJ, 120, 511
Reese E. D., et al., 2012, ApJ, 751, 12
Reid B. A., Spergel D. N., 2006, ApJ, 651, 643
Richard J., Kneib J.-P., Limousin M., Edge A., Jullo E., 2010, MNRAS, 402, L44
Riebe K., et al., 2013, Astronomische Nachrichten, 334, 691
Rines K., Geller M. J., Diaferio A., Kurtz M. J., 2013, ApJ, 767, 15
Rines K. J., Geller M. J., Diaferio A., Hwang H. S., 2016, ApJ, 819, 63
Rozo E., et al., 2010, ApJ, 708, 645
Rozo E., Rykoff E. S., Bartlett J. G., Evrard A., 2014a, MNRAS, 438, 49
Rozo E., Evrard A. E., Rykoff E. S., Bartlett J. G., 2014b, MNRAS, 438, 62
Ruel J., et al., 2014, ApJ, 792, 45
Saro A., Mohr J. J., Bazin G., Dolag K., 2013, ApJ, 772, 47
Sehgal N., et al., 2011, ApJ, 732, 44
Sehgal N., et al., 2013, ApJ, 767, 38
Shaw L. D., Holder G. P., Bode P., 2008, ApJ, 686, 206
Sifón C., et al., 2013, ApJ, 772, 25
Skibba R. A., van den Bosch F. C., Yang X., More S., Mo H., Fontanot F., 2011, MNRAS, 410, 417
Skielboe A., Wojtak R., Pedersen K., Rozo E., Rykoff E. S., 2012, ApJL, 758, L16
Soucail G., Mellier Y., Fort B., Cailloux M., 1988, A&AS, 73, 471
Springel V., 2005, MNRAS, 364, 1105
Springel V., White M., Hernquist L., 2001, ApJ, 549, 681
Springel V., et al., 2005, Nature, 435, 629
Sunyaev R. A., Zeldovich I. B., 1980, ARA&A, 18, 537
Swetz D. S., et al., 2011, ApJS, 194, 41
VanderPlas J., Connolly A. J., Ivezic Z., Gray A., 2012, in Proceedings of Conference on Intelligent Data Understanding (CIDU), pp. 47-54, 2012.. pp 47–54 (arXiv:1411.5039), doi:10.1109/CIDU.2012.6382200
Vikhlinin A., et al., 2009, ApJ, 692, 1060
Viola M., et al., 2015, MNRAS, 452, 3529
Wen Z. L., Han J. L., 2013, MNRAS, 436, 275
White M., Cohn J. D., Smit R., 2010, MNRAS, 408, 1818
Wik D. R., Sarazin C. L., Ricker P. M., Randall S. W., 2008, ApJ, 680, 17
Wojtak R., Łokas E. L., Mamon G. A., Gottlöber S., Prada F., Moles M., 2007, A&A, 466, 437
Wright E. L., et al., 2010, AJ, 140, 1868
Wu H.-Y., Hahn O., Evrard A. E., Wechsler R. H., Dolag K., 2013, MNRAS, 436, 460
Yu L., Nelson K., Nagai D., 2015, ApJ, 807, 12
Zel'dovich Y. B., Sunyaev R. A., 1969, Ap&SS, 4, 301
Zitrin A., Menanteau F., Hughes J. P., Coe D., Barrientos L. F., Infante L., Mandelbaum R., 2013, ApJL, 770, L15
da Silva A. C., Kay S. T., Liddle A. R., Thomas P. A., 2004, MNRAS, 348, 1401
van Dokkum P. G., 2001, PASP, 113, 1420
von der Linden A., et al., 2014a, MNRAS, 439, 2
von der Linden A., et al., 2014b, MNRAS, 443, 1973

APPENDIX A: EDDINGTON BIAS AND SELECTION EFFECTS

In this appendix we discuss the SZ and dynamical mass measurements in the context of understanding potential biases, such as Eddington bias (Eddington 1913), that might affect the comparison of the two mass proxies. We then demonstrate with a simple simulation that the method used in Section 3.4 to determine the ratio $(1 - b_{\rm SZ})/\beta_{\rm dyn}$ is unbiased.

The SZ masses used in this work have been corrected for Eddington bias by Hasselfield et al. (2013). The calculation accounts for the fact that the underlying mass function is falling steeply as mass increases, so a direct inversion of $y_{\rm SZ}(M)$ gives a biased estimate of $M(y_{\rm SZ})$ (Evrard et al. 2014). The computation of the correction requires certain assumptions, such as the form of the cluster mass function and the survey selection function, which is constructed assuming a particular model for the SZ signal and an assumption about the degree of intrinsic scatter. Under these assumptions the correction is then computed in a Bayesian framework, with the posterior probability of a cluster's mass given by $P(M|y) \propto P(y|M)n(M)$, where the likelihood $P(y|M)$ accounts for

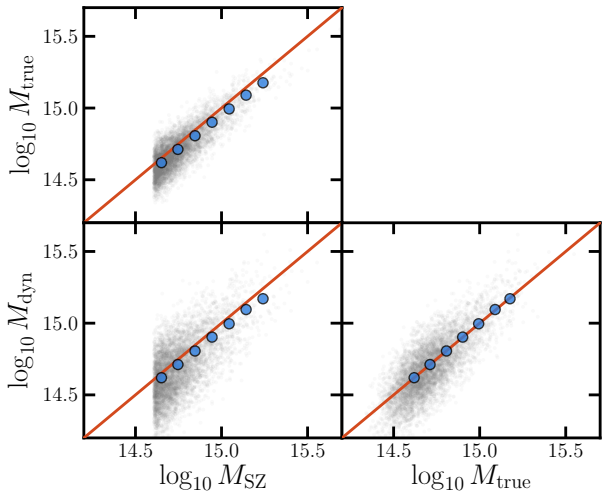

Figure A1. Comparison of SZ, dynamical, and true cluster masses for a mock catalog that incorporates a simple model for noise, scatter and selection effects. The gray points are individual mock clusters. The blue points show the mean masses for several bins in $M_{\rm SZ}$. Because the binning is based on the measured $M_{\rm SZ}$ value, the binned $M_{\rm SZ}$ are consistently higher than the binned $M_{\rm true}$ (upper left panel). In contrast, the $M_{\rm dyn}$ are not affected by Eddington bias (lower right panel) and lie on the $y = x$ (red) line.

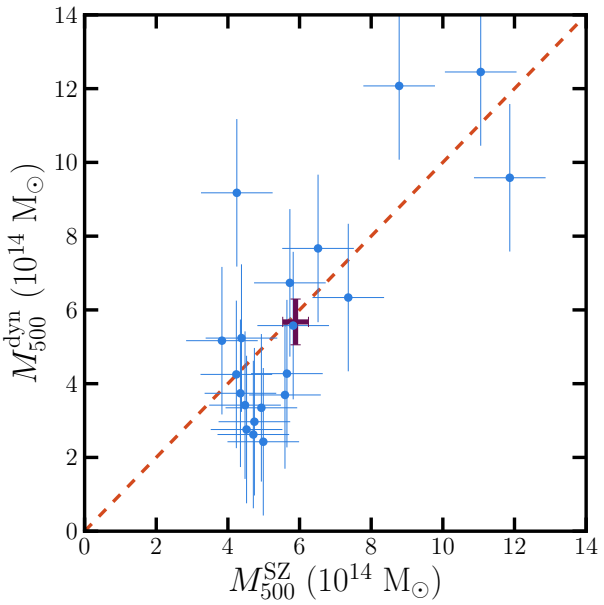

Figure A2. Masses of 20 clusters drawn from a large mock catalog that simulates noise, scatter, and selection effects. Purple cross shows the mean characteristic SZ and dynamical mass, computed under uniform weights. As in Figure 6, errorbars in the individual cluster masses include only the noise contribution and not intrinsic scatter.

intrinsic scatter and measurement noise and the prior $n(M)$ is the cluster mass function (see section 3.2 of Hasselfield et al. 2013).

Aside from the modelling assumptions, it is important to note that the correction is no longer valid if we change the underlying distribution of cluster masses upon which the ACT selection is effectively acting. For example, if we were to remove objects from the sample based on some auxiliary information (such as X-ray flux, or membership in an optical cluster survey), then we would risk complicating the underlying mass function and invalidating the Eddington bias correction applied in Hasselfield et al. (2013).

However, there are many ways to sub-sample the ACT sample without changing the validity of the Eddington bias correction. Restricting the survey to a smaller region of the sky, or to a particular redshift range[21] does not affect the Eddington bias correction. Although less obvious, it is also true that raising the S/N threshold of the catalog does not change the correction (though of course this will change the membership of the sample). While the S/N threshold affects the survey selection function (which we take to mean the probability that a cluster of some mass and redshift would be included in the sample), it does not affect the underlying distribution of masses which we should consider when working with a particular cluster that has been detected. In a Bayesian framework, the posterior distribution for any one cluster's mass is not dependent on the overall survey selection function. The cosmological sample considered in this work satisfies the requirements above, and so we take the masses of Hasselfield et al. (2013), which have been corrected for Eddington bias, to be unbiased on average.

The dynamical masses presented in this work were obtained for all clusters passing certain redshift and S/N cuts (i.e., those in the cosmological sample of Hasselfield et al. 2013), and the present measurements were not used to refine the sample further. Though noise and scatter will certainly affect the velocity dispersion measurements, we expect positive and negative noise (or scatter) excursions to be equally likely. The dynamical mass measurements thus constitute a complete set of "follow-up" observations for the sample, and are not affected by Eddington bias.

While the descriptions above can be justified formally (see Evrard et al. 2014), we illustrate their validity using mock catalogs of SZ and dynamical mass measurements. We draw a large number of masses, $M_{\rm true}$, from a realistic cluster mass function, considering a single redshift. We create SZ and dynamical mass proxy measurements by adding intrinsic scatter (at the 20 and 30 per cent levels, respectively) and measurement noise (fixed at $10^{14}\,M_\odot$ and $2\times10^{14}\,M_\odot$, respectively) to the true masses. Then we simulate the effect of SZ selection by keeping only mock clusters with $M_{\rm SZ} > 4\times10^{14} M_\odot$.

In Figure A1 we show these mock clusters, and demonstrate that if we bin the objects according to their $M_{\rm SZ}$ measurement, we see Eddington bias effects in $M_{\rm SZ}$ relative to the true cluster mass, but $M_{\rm dyn}$ is not biased. In the real observations, the Eddington bias in $M_{\rm SZ}$ is corrected by modeling the mass function and SZ scaling relation. For the mock study we simply fit a constant bias factor to the binned $M_{\rm SZ}$ and M_{true} points and use it to correct the individual mock $M_{\rm SZ}$ values.

We then take a random subsample consisting of 20 mock clusters, to roughly match the size of the real sample considered in this work. We compute the characteristic SZ and dynamical mass of these clusters, under uniform weights, as was done in Section 3.5. The resulting ratio is consistent, as expected, with unity. This subsample and the characteristic masses are plotted in Figure A2.

We also repeat the entire procedure for alternative weighting schemes. We find that weighting schemes that incorporate the measured dynamical masses are significantly biased. For example, if we take the weights to be the inverse square of the combined measurement error and intrinsic scatter, the characteristic dynamical

[21] The redshift cut can in principle affect the bias correction due to uncertainty in the cluster redshifts; in practice the redshift uncertainties are small enough that this is not significant.

mass is 10 per cent lower, on average, than the characteristic SZ mass. Such biases are also seen in weights that include the fractional measurement error (which requires the input of the measured mass), or weights that incorporate the intrinsic scatter contribution (which scales in proportion to the measured mass). The real data contain additional correlations between dynamical mass and measurement error beyond those modeled in this simple simulation, because more massive clusters also tend to have more galaxies that can be used to measure the dispersion. For these reasons it is clear that one should not incorporate the dynamical mass measurements and errors into the weights unless the impact can be fully modelled.

In constrast, for this simulation we find that weighting by the inverse square of the SZ mass error (including the contribution from intrinsic scatter) does not bias the mass comparison. This is because we have already corrected the SZ masses to make them unbiased, even under weights (or selection choices) that depend on the measured SZ mass.

APPENDIX B: VELOCITY HISTOGRAMS AND REDSHIFT CATALOGUE

We show in Figures B1 and B2 the velocity histograms for all clusters (only member galaxies are shown). We show histograms with bins of $400\,\mathrm{km\,s^{-1}}$ and with a constant bin size that maximizes the predictive power of the histogram in a Bayesian sense (Knuth 2006)[22].

Table B1 presents the redshift measurements for all galaxies that enter the analysis. We include both members and non-members to allow for reproducibility and independent analyses to be carried out with these data. All redshifts are in the heliocentric frame. Note that this is not the case in the redshift catalogue published by Sifón et al. (2013). We therefore include redshifts for galaxies in the southern survey here for consistency.

This paper has been typeset from a TEX/LATEX file prepared by the author.

[22] We use the version implemented in the `plotting` library of `astroML` (VanderPlas et al. 2012).

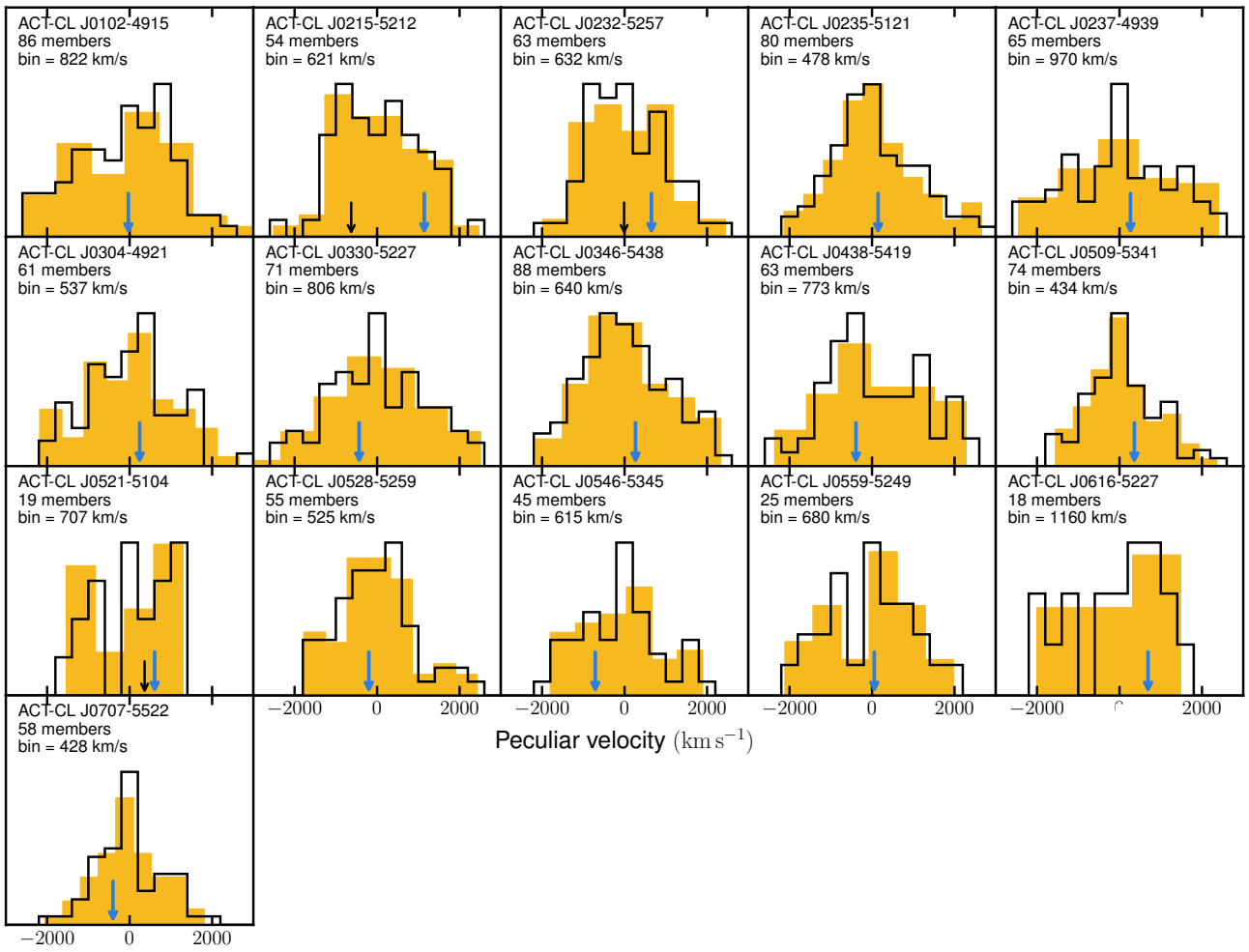

Figure B1. Velocity histograms of all clusters in the southern sample. Black empty histograms have a bin size of 400 km s^{-1} and filled yellow histograms have a bin size indicated in the legend, which is such that the predictive power of the histogram (i.e., the likelihood that the next datum will fall in a given bin) is maximized using a bayesian approach. We show normalized counts and list the number of members in each cluster in the legends (see also Table 2). Blue arrows mark the BCG velocities and, where applicable, smaller black arrows mark peculiar velocities of alternative choices for the BCG (see Sections 3.7 and 4). BCG velocities have a typical uncertainty of ≈ 100 km s^{-1}.

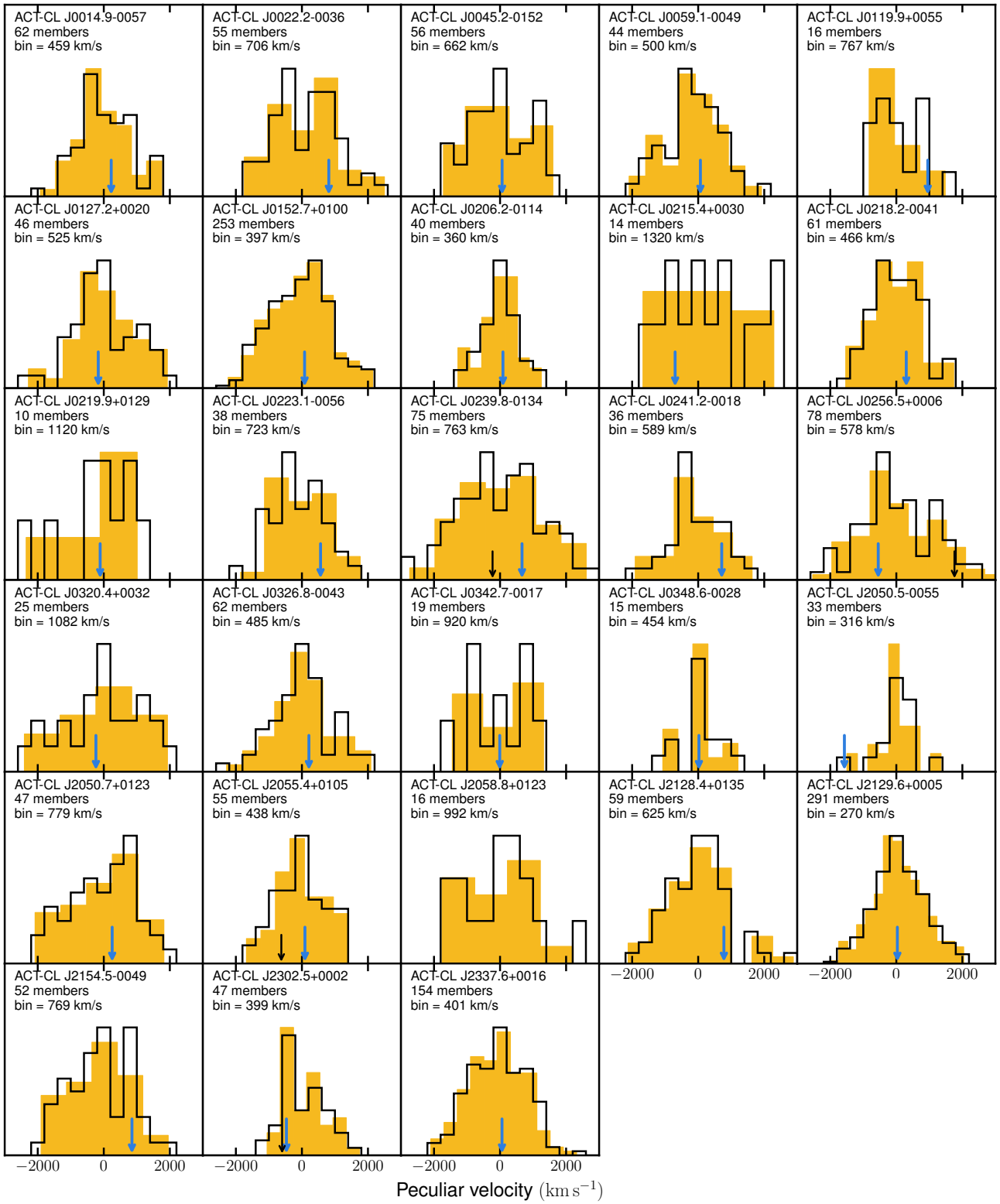

Figure B2. Rest-frame velocity histograms of all clusters in the equatorial sample. Styles are the same as Figure B2. We do not know the redshift of the BCG of ACT-CL J2058.8+0123.

Table B1. BCGs of the 44 ACT SZ-selected clusters studied in this work. The full spectroscopic catalog will be available in the online version of the journal. A portion is shown here for guidance regarding its form and content. Columns are: (1): catalogue designation (BCGs are marked with asterisks); (2), (3): J2000 coordinates; (4), redshift and nominal uncertainty; (5): membership flag (1: member, 0: non-member); (6): spectroscopic source. References are: (1) Gemini/GMOS (this work), (2) Gemini/GMOS (Sifón et al. 2013), (3) VLT/FORS2 (Sifón et al. 2013), (4) SALT/RSS (Kirk et al. 2015), (5) SDSS DR12 (**?**), (6) HeCS (Rines et al. 2013), (7) Soucail et al. (1988), (8) Dressler et al. (1999).

Name	RA	Decl.	z	Member?	Source
J001454.10−005708.4*	00:14:54.10	−00:57:08.4	0.53435 ± 0.00035	1	1
J002213.03−003633.8*	00:22:13.03	−00:36:33.8	0.80960 ± 0.00031	1	1
J004512.49−015231.6*	00:45:12.49	−01:52:31.6	0.54862 ± 0.00023	1	1
J005806.10+003050.0*	00:58:06.10	+00:30:50.0	0.79223 ± 0.00029	1	1
J005908.50−005005.7*	00:59:08.50	−00:50:05.7	0.78740 ± 0.00018	1	1
J011958.14+005533.6*	01:19:58.14	+00:55:33.6	0.73690 ± 0.00015	1	1
J012716.64+002040.9*	01:27:16.64	+00:20:40.9	0.37933 ± 0.00023	1	1
J015241.95+010025.5*	01:52:41.95	+01:00:25.5	0.22953 ± 0.00012	1	6
J015624.29−012317.3*	01:56:24.29	−01:23:17.3	0.45260 ± 0.00039	1	4
J020613.14−011500.0*	02:06:13.14	−01:15:00.0	0.67629 ± 0.00014	1	1
J021527.94+003050.0*	02:15:27.94	+00:30:50.0	0.85786 ± 0.00031	1	1
J021816.88−004141.8*	02:18:16.88	−00:41:41.8	0.67448 ± 0.00020	1	1
J021952.15+012952.1*	02:19:52.15	+01:29:52.1	0.36460 ± 0.00039	1	4
J022310.05−005709.0*	02:23:10.05	−00:57:09.0	0.66633 ± 0.00015	1	1
J023952.74−013418.9*	02:39:52.74	−01:34:18.9	0.37815 ± 0.00000	1	7
J024115.44−001841.0*	02:41:15.44	−00:18:41.0	0.69121 ± 0.00029	1	1
J025633.76+000628.8*	02:56:33.76	+00:06:28.8	0.36001 ± 0.00013	1	1
J032029.78+003153.6*	03:20:29.78	+00:31:53.6	0.38360 ± 0.00039	1	4
J032649.95−004351.7*	03:26:49.95	−00:43:51.7	0.44812 ± 0.00004	1	1
J034242.65−001708.3*	03:42:42.65	−00:17:08.3	0.30716 ± 0.00005	1	5
J034839.54−002816.8*	03:48:39.54	−00:28:16.8	0.34500 ± 0.00039	1	4
J205029.76−005540.6*	20:50:29.76	−00:55:40.6	0.61409 ± 0.00032	0	1
J205043.13+012329.2*	20:50:43.13	+01:23:29.2	0.33503 ± 0.00036	1	1
J205523.25+010607.5*	20:55:23.25	+01:06:07.5	0.40933 ± 0.00023	1	1
J212823.42+013536.4*	21:28:23.42	+01:35:36.4	0.38920 ± 0.00012	1	1
J212939.96+000521.1*	21:29:39.96	+00:05:21.1	0.23393 ± 0.00013	1	6
J215432.35−004900.4*	21:54:32.35	−00:49:00.4	0.49454 ± 0.00027	1	1
J230235.05+000234.2*	23:02:35.05	+00:02:34.2	0.51666 ± 0.00018	1	1
J233739.72+001616.9*	23:37:39.72	+00:16:16.9	0.27715 ± 0.00018	1	6
J010257.74−491619.2*	01:02:57.74	−49:16:19.2	0.86991 ± 0.00030	1	3
J021512.26−521225.2*	02:15:12.26	−52:12:25.2	0.48595 ± 0.00016	1	2
J023249.47−525711.1*	02:32:49.47	−52:57:11.1	0.55948 ± 0.00034	1	2
J023545.28−512105.0*	02:35:45.28	−51:21:05.0	0.27813 ± 0.00015	1	2
J023701.71−493809.9*	02:37:01.71	−49:38:09.9	0.33548 ± 0.00016	1	2
J030416.03−492126.2*	03:04:16.03	−49:21:26.2	0.39283 ± 0.00020	1	2
J033056.83−522813.8*	03:30:56.83	−52:28:13.8	0.43961 ± 0.00019	1	2
J034655.49−543854.9*	03:46:55.49	−54:38:54.9	0.53105 ± 0.00013	1	2
J043817.70−541920.6*	04:38:17.70	−54:19:20.6	0.41935 ± 0.00012	1	2
J050921.38−534212.2*	05:09:21.38	−53:42:12.2	0.46196 ± 0.00022	1	3
J052114.54−510418.4*	05:21:14.54	−51:04:18.4	0.67719 ± 0.00041	1	2
J052805.30−525952.8*	05:28:05.30	−52:59:52.8	0.76632 ± 0.00037	1	3
J054637.67−534531.3*	05:46:37.67	−53:45:31.3	1.06190 ± 0.00016	1	3
J055943.23−524927.1*	05:59:43.23	−52:49:27.1	0.60969 ± 0.00027	1	3
J061634.05−522710.0*	06:16:34.05	−52:27:10.0	0.68759 ± 0.00011	1	2
J070704.67−552308.5*	07:07:04.67	−55:23:08.5	0.29405 ± 0.00019	1	2